7-2009

Comparison of a-Fe2O3 electrodes grown by direct plasma and thermal oxidation of iron for photoelectrochemical water splitting.

Boris David Chernomordik
University of Louisville

COMPARISON OF α-Fe_2O_3 ELECTRODES GROWN BY DIRECT PLASMA AND THERMAL OXIDATION OF IRON FOR PHOTOELECTROCHEMICAL WATER SPLITTING

By

Boris David Chernomordik

B.S., University of Louisville, 2008

A Thesis

Submitted to the Faculty of the

University of Louisville

J.B. Speed School of Engineering

as Partial Fulfillment of the Requirements

For the Professional Degree

MASTER OF ENGINEERING

Department of Chemical Engineering

July 2009

COMPARISON OF α-Fe_2O_3 ELECTRODES GROWN BY DIRECT PLASMA AND THERMAL OXIDATION OF IRON FOR PHOTOELECTROCHEMICAL WATER SPLITTING

By

Boris David Chernomordik

B.S., University of Louisville, 2008

A Thesis

Submitted to the Faculty of the

University of Louisville

J.B. Speed School of Engineering

as Partial Fulfillment of the Requirements

For the Professional Degree

MASTER OF ENGINEERING

Department of Chemical Engineering

July 2009

COMPARISON OF α-Fe_2O_3 ELECTRODES GROWN BY DIRECT PLASMA AND THERMAL OXIDATION OF IRON FOR PHOTOELECTROCHEMICAL WATER SPLITTING

Submitted by:_____

Boris David Chernomordik

A Thesis Approved on

_____

(Date)

By the Following Reading and Examination Committee:

_____

Mahendra K. Sunkara, PhD, Thesis Director

_____

Moises A. Carreon, PhD

_____

Richard P. Baldwin, PhD

ACKNOWLEDGEMENTS

The author acknowledges his thesis director, Dr. Mahendra Sunkara, for his guidance, persistence, optimism, enthusiasm, and support throughout the past four and half years. The author thanks Drs. Moises Carreon and Richard Baldwin for their willingness and time in participating in the examination. The author would also like to thank Dr. Jacek Jasinski for his assistance during the project. The author also thanks his fellow graduate students for their support. The author is also grateful to Kentucky Space Grant Consortium and the University of Louisville for their financial support over the past year. The author is also immeasurably grateful to his family and friends for their love and support.

ABSTRACT

Iron oxide, Fe_2O_3, is a promising material for water splitting reaction using solar energy due to its stability and optimal bandgap of 2 eV. Even the recent efforts, however, using Fe_2O_3 thin film materials reported low efficiencies due to poor carrier transport within these films.

A novel plasma oxidation method was used to synthesize arrays of α-Fe_2O_3 which are single crystal and have highly ordered oxygen vacancy planes. As one-dimensional nanostructures, these nanowires offer many other benefits to photoelectrochemical electrolysis, including high surface area, reduced charge carrier diffusion distance, and a preferential direction for charge diffusion. Furthermore, due to the ordered-oxygen vacancy planes in these nanowires, the high resistivity that has plagued this material may become a non-issue.

The photoelectrochemical performance of these samples was compared to that of nanowire (and nanobelt) arrays grown by thermal oxidation of iron foils. Hematite samples grown by plasma oxidation were found to have considerably greater photoactivity than by thermal oxidation. This was attributed to the presence of a large (7.5 μm) mixed-phase interfacial layer in the latter, wherein the charge carriers are lost to recombination. Due to the fast growth process in plasma oxidation, the interfacial layer is much thinner (1 μm) and may in fact contain only hematite, rather than a mixed phase. Studies are currently underway to determine the interfacial layer composition.

It is concluded that further studies of hematite for photoelectrochemical electrolysis should be performed using nanowire arrays grown by direct plasma oxidation.

TABLE OF CONTENTS

LIST OF FIGURES

I. INTRODUCTION AND MOTIVATION

Energy is one of the most fundamental societal necessities. Currently, we are facing a global problem with regard to sources of energy. The global energy demand is 13+ TW (as of 2001), and is ever increasing. That is approximately equivalent to the energy output of an astounding 13000 nuclear power plants. A large majority of our current energy supply and consumption is dominated by fossil fuels (oil, coal, natural gas)[1, 2]. These resources are nearing their limits, poisoning the environment, hurting our health, and contributing to international conflicts. Energy is tied to every aspect of society. For example, scarcity causes cost spikes which contribute to slowing economic growth, begetting social upheaval. Energy should be cheap, clean, and globally available: cheap because it is the foundation for all other development, clean to avoid health problems and associated costs and to minimize impact on the environment, and globally available so that a few nations never hold the world's energy supply for ransom.

Several alternative energy sources are available, including solar-derived, wind, geothermal, biomass, hydro, wave, nuclear and hydrogen. Geothermal, hydro, and wave are very clean but site-specific resources that may benefit a local region but cannot begin to address the global energy demand. Biomass, though promising, should not compete with the global agriculture, agriculture-dependent industries, such as feedstock and fertilizer, or put pressure on utilization of protected lands. There may also be issues regarding harmful emissions from burning biofuels as well as whether the energy output is greater than the energy input. Satisfying the global energy needs with nuclear technology would require an astonishing number of nuclear plants, together producing a large quantity of nuclear waste endangering the safety and health of local populations for

many generations. Another issue is that global uranium resources are limited. Solar and wind are capable of meeting significant energy demands. Solar alone can fulfill our energy requirements. The amount of energy falling on our planet is roughly equivalent to 1.2×10^5 TW, enough to meet our global energy demand many times over for many years to come. The vast portion of that energy is wasted, such as on heating parking lots, however. Solar and wind collecting devices are capable of supplying energy for immediate use, but must be coupled with an energy storage device to provide energy during the times when there is no sunlight or wind. Batteries are an expensive solution which has a number of technical and practical obstacles. Hydrogen is chemically stored energy. When converted to electricity in a fuel cell, coupling hydrogen derived from the electrochemical splitting of water with a renewable energy source is the cleanest possible fuel.

The byproducts of electrochemical splitting of water are hydrogen and oxygen gases. These may be recombined in a fuel cell to produce water and electricity. It is in essence a closed loop fuel cycle, except that energy must be put in and out. If that energy input is solar radiation, then the result is a clean and possibly inexhaustible energy supply. One method of obtaining hydrogen electrochemically involves an electrolyzer—powered by solar panels, for example. Commercial electrolyzers typically use platinum, an expensive and precious metal. This two-part operation would add significantly to the capital involved in collecting hydrogen. Instead, there is significant interest in semiconductor-based devices that can harness solar radiation to drive the electrochemical water splitting reaction on the semiconductor surface. In fact, direct

photoelectrochemical (PEC) water splitting using sunlight is described as the “Holy Grail” of electrochemistry[3, 4].

II. THEORY

Photoelectrolysis

The following net reaction describes the electrolysis of water:

$$2H_2O(l) \leftrightarrow 2H_2(g) + O_2(g) \qquad \Delta E^o = -1.23 \text{ eV} \qquad (1)$$

It is composed of two half-reactions. Hydrogen gas is produced at the cathode by the reduction half-reaction, which is defined as 0V on the electrochemical scale when it occurs in pH = 0:

$$2H^+(aq) + 2e^- \leftrightarrow H_2(g) \qquad E^o = 0.00 \text{ eV} \qquad (2)$$

This electrochemical reference point is defined as the Normal Hydrogen Electrode (NHE) potential. Oxygen gas is evolved on the anode during the oxidation half-reaction:

$$2H_2O(l) \leftrightarrow O_2(g) + 4H^+(aq) + 4e^- \qquad E^o = -1.23 \text{ eV} \qquad (3)$$

These reactions occur at the two respective electrodes. Thus, simple physical separation may allow the gases to be collected and stored separately.

This electrolysis is a non-spontaneous reaction, which means that it requires energy input. As shown in Equation (1), the minimal energy requirement is 1.23 eV. Using the following relation:

$$\lambda = \frac{hc}{eE}, h = 6.625 \cdot 10^{-34} J \cdot s, c = 2.998 \cdot 10^{17} \frac{nm}{s}, e = 1.60 \cdot 10^{-19} C \qquad (4)$$

(where λ is wavelength in nanometers, h is Planck's constant, c is the speed of light in vacuum, e is the electronic charge magnitude, and E is the energy of the photon in eV), the energy requirement to split water corresponds to radiation with a wavelength of 1010 nm. Photons with energy greater than 1.23 eV (or wavelength less than 1010 nm), which encompass the visible light spectrum, can drive the electrolysis reaction. The integrated solar irradiance is Earth's atmosphere filters portions of the solar spectrum and the radiation intensity decreases as distance light travels through the atmosphere increases (in adherence to the Beer-Lambert Law). The "AMX" (air mass) standard was developed to reflect this effect, where "X" is the air mass coefficient:

$$X = \frac{I}{I_0} = \frac{I_0}{I_0 cos\theta} = \frac{1}{cos\theta} \quad (5)$$

where I_0 is the light intensity before entering the atmosphere, I is the intensity after light travels a particular distance through the atmosphere, and θ is the solar zenith angle—measured between the straight path of light to a point and the normal. The following are the air mass conventions and their meanings: AM0 for the solar flux in space, AM1 for the terrestrial solar flux normal to the surface, and AM1.5 for the terrestrial solar flux at a zenith angle of 48.2º. AM1.5 is the accepted standard for solar cell analysis and reflects the day-average solar radiation, with the irradiance rounded to 1000 W/m^2. The AM0 and AM1.5 solar spectra are shown in Figure 1.

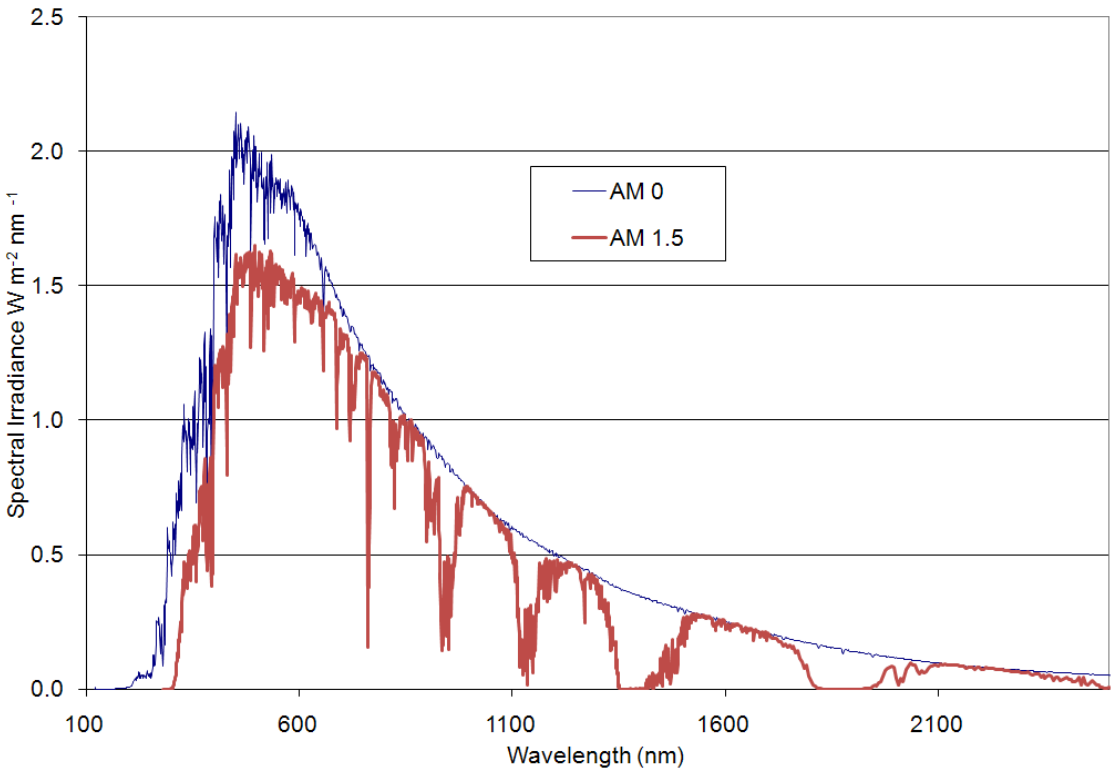

Figure 1. Solar spectra corresponding to AM0 and AM1.5 standards[5].

Semiconductor materials are capable of absorbing light energy to drive an electrochemical reaction. Semiconductors may also be used to perform photolysis, the decomposition of a chemical compound using a photoactive catalyst, for a number of applications including decomposition of hazardous waste. A significant amount of research in this area is devoted to solar fuels, particularly photoelectrochemical electrolysis for hydrogen generation.

The fundamental components of a PEC cell are the cathode and anode, both or either of which may be a semiconductor. If the anode is a photoactive semiconductor material, then it is called a photo-anode. N-type semiconductors are photo-anodes because they drive the water oxidation reaction; p-type semiconductors are photo-

cathodes because they drive the reduction reaction (detailed explanation may be found later in the text). If only one electrode is a semiconductor, it is considered the working electrode (WE) and a noble metal is typically chosen to serve as the counter electrode (CE). A third electrode, the reference electrode (RE), is also commonly when testing PEC performance of a semiconductor. In a two-electrode cell, the potentiostat applies a bias between the WE and CE, but one does not know how the bias is distributed between the two electrodes. In a three electrode measurement, the desired bias is applied to the WE with respect to the RE. Thus, in the latter case, potential on the WE is known. The bias on the CE, however, varies according to the flow of charges. Three electrode measurements do not indicate the bias between the WE and the CE. That has to be determined by connecting a multimeter. Essentially, a three electrode measurement focuses on the behavior of the WE and does not report what is happening at the CE. A common reference electrode is Ag/AgCl. Figure 2 illustrates a typical three-electrode PEC cell involving a photo-anode WE, platinum CE, and a reference electrode (RE). Upon illumination by sunlight, the generated electrons flow from the bulk of the photo-anode to the cathode, whereupon they participate in the evolution of hydrogen. The positively charged holes oxidize water at the surface of the photo-anode to produce oxygen and positive ions.

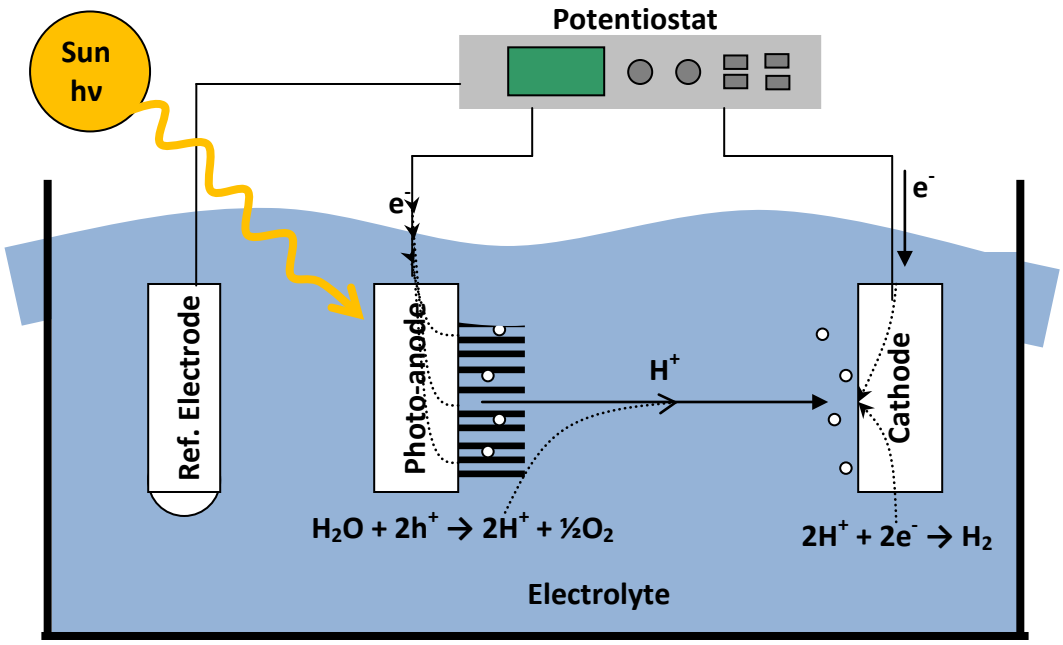

Figure 2. An illustration of a three-electrode photoelectrochemical water splitting system in which the photo-anode is the semiconductor nanowire array. "h^+" represents an electron-hole and "e^-" represents an electron.

Semiconductor Principles:

The conductivity type of a semiconductor (n-type or p-type) is determined by its Fermi level position. A characteristic property of semiconductors is the band gap (E_g), an energy minimum representing the separation between the valence and conduction bands, as illustrated in Figure 3. The promotion of an electron from the valence band—also called the highest occupied molecular orbital (HOMO)—to the conduction band—or, lowest unoccupied molecular orbital (LUMO)—occurs and the electron is free to move within the lattice. Consequently, the free-electron leaves behind a hole—a positive charge signifying the absence of an electron—in the valence band. The hole is also free to move within the lattice, through the propagation of a free electron, in the opposite direction. In the case of a direct band gap semiconductor, energy input equal to or greater

than E_g will allow an electron to conduct through the lattice. Some materials exhibit an indirect band gap, however. Although the band gap is still the minimum separation between the valence band maximum and the conduction band minimum, these points are offset by a finite momentum, p. Mathematically, the bands are represented by a parabolic relationship between energy, E, and crystal momentum, k:

$$E - E_c \;\; or \;\; Ev - E = \frac{p^2}{2m} = \frac{\hbar^2 k^2}{2m} \tag{6}$$

where m is the effective mass of the particle (m_e^* for electron in E_c and m_h^* for hole in E_v), and $\hbar$ is the reduced Planck's constant ($\hbar=\frac{h}{2\pi}$). Equation (6), represents a free particle, but the relationship becomes complex in an actual crystal because of particle interaction with the atoms and due to crystal structure and direction. Figure 4 shows an E versus k band diagram for a hypothetical semiconductor material with a direct band gap (a) and an indirect band gap (b). As before, the upper line is the conduction band and the lower line is the valence band. In 5a, the conduction band minimum lines up with the valence band maximum along k=0. This is the case for direct band gap materials, such as GaAs, and it is an important feature for applications in optical devices including light emitting diodes. In 5b, the conduction band minimum occurs along the [100] crystal direction, rather than at k=0. In this case, an interaction with the crystal is necessary for an electron to transition from E_v to E_c. The measure of this interaction is a phonon, a quantized measure of a crystal lattice vibration. Therefore, the crystal must absorb a photon with an energy E_g and a phonon, or heat. An indirect band gap material can also experience a direct transition if the absorbed energy is equivalent to the gap at k=0. Silicon is an example of an indirect band gap material, which has nonetheless found wide

acceptance for photovoltaics out of commercial practicality. Light can penetrate farther into an indirect band gap material without exciting an electron across the band gap because absorption of a photon and phonon must happen simultaneously. This is why silicon solar cells are typically hundreds of microns thick.

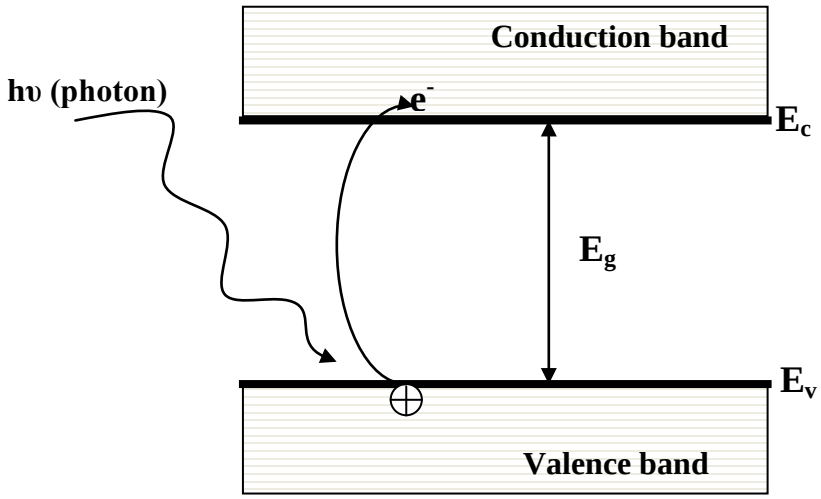

Figure 3. Schematic showing the excitation of an electron from the valence band to the conduction band.

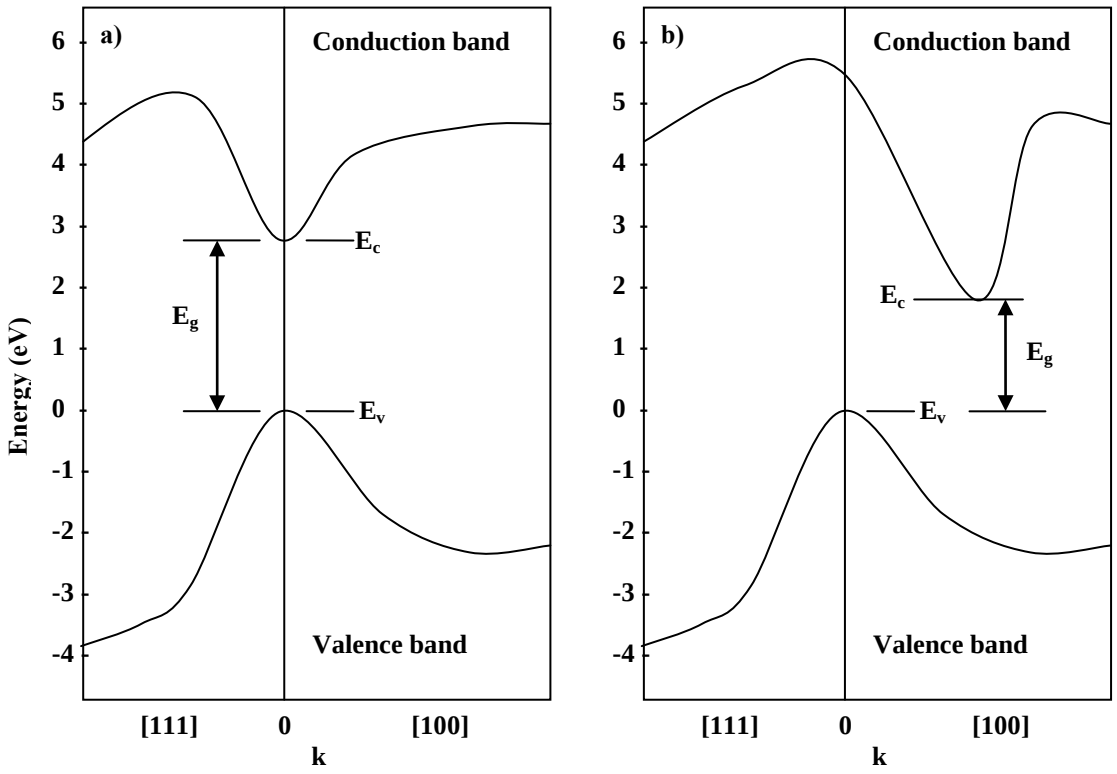

Figure 4. A schematic of the energy versus momentum (k) diagram for direct (a) and indirect (b) band gap semiconductors.

The conduction and valence bands are simply two states which charges may occupy, but there exists a density of states above and below, respectively, which may be occupied. The probability of these states being occupied is represented by the Fermi-Dirac distribution function:

$$\frac{N(E)}{g(E)} = f_F(E) = \frac{1}{1+\exp\left(\frac{E-E_F}{kT}\right)} \qquad (7)$$

Where N(E) is the number of particle (electrons) per unit volume per unit energy, g(E) is the density of quantum states (number per unit volume) per unit energy, k is the Boltmann constant, and T is temperature in Kelvin. When $E=E_F$, the Fermi energy, the

Fermi-Dirac distribution is equal to ½, or 50%. The Fermi energy is not an occupiable state, but it does represent an energy level has a 50% probability of being occupied. In electrochemistry, the Fermi level is the electrochemical potential (μ) of electrons in the semiconductor solid. For a simple redox couple, the Fermi level is given by:

$$E_{F,redox} = \bar{\mu}_{e,redox} = \mu^{\circ}_{redox} + kTln\left(\frac{c_{ox}}{c_{red}}\right) \quad (8)$$

where c_{ox} and c_{red} are the concentrations of oxidized and reduced species. For a simple visual interpretation one can imagine that the Fermi level would nearer the band edge where with the highest concentration of electrons (in the case of E_c) or holes (in the case of E_v).

Introducing donor or acceptor states can shift the Fermi level and so define the conductivity type of a semiconductor (n- or p-type). In an intrinsic semiconductor, such as undoped silicon, the Fermi level is at midgap between the conduction and valence bands. "Impurity" atoms introduced into a crystal lattice can donate electrons or holes. For example, doping silicon with phosphorous atoms creates n-type silicon. Whereas silicon has four valence electrons, phosphorous has five, thus it is capable of donating an electron to the crystal—like water poured from the top of a hill jutting out of the ocean. For p-type, the dopant atom has fewer valence electrons than the atoms surrounding it and thus acts as an acceptor of electrons from the crystal. For doping, the concentration of impurity atoms in the crystal is typically on the order of 10^{15} to 10^{19} cm^{-3}. The presence of dopants influences the distribution of charge carriers below and above the band gap. For n-type semiconductors, the density of occupied states above the conduction band is increased, and consequently the Fermi level rises nearer to the

conduction band. For p-type, the Fermi level is nearer the valence band. This is schematically shown in Figure 5. Reference [6] pertains to the above discussion.

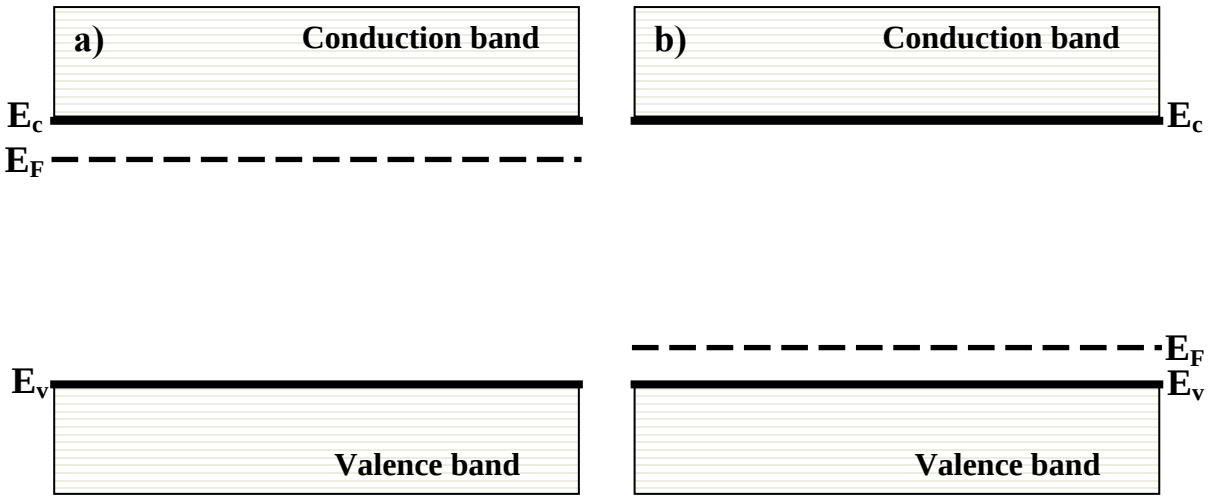

Figure 5. A schematic of the Fermi level position in n-type (a) and p-type (b) semiconductors.

In the presence of an electrolyte, the semiconductor Fermi level equilibrates with that of the electrolyte[7, 8]. The energy levels for a photoanode and metal cathode before contact, in dark, and under illuminations are shown in Figure 6. These schematics plot voltage on an electrochemical scale (up = negative, 0 = NHE) versus a single space dimension. Thus, when referring to the band diagram, a rise corresponds to a negative potential shift, and vice versa. The electrolyte Fermi level is somewhere between the O_2/H_2 redox couple—depending on the concentration—and is a function of the Gaussian type distribution of redox states, which is detailed further in a number of review articles[7, 9-11]. In the case of an n-type, the electrochemical potential is greater within the semiconductor than in the electrolyte. As a result, electrons diffuse from the solid surface into the solution. This leaves the semiconductor surface positively ionized, creating a space charge region. Consequently, oppositely charged ions congregate on the

electrolyte side of the interface, creating a charge double layer called the Helmholtz layer. On the band diagram, this effect is represented by the bending of the conduction and valence bands. The band edge positions at the interface are pinned and do not change throughout the interaction because they are a function of the Helmholtz layer parameters, which depend on the specific material-electrolyte interaction. The bulk of the semiconductor does not "see" the Helmholtz layer, however, and may experience a redistribution of electrochemical potential. This is manifested by the shifting of the Fermi level, which is a bulk material property. The energy gaps between the band edges and the Fermi level are functions of the material and remain constant, forcing the bands to move in congress with the Fermi level. The space charge region where the bands are bent contains an electric field, the direction of which is determined by the relative position of the Fermi level to the electrolyte redox potential. In an n-type semiconductor, the bands shift downward (more positive) in order to reach equilibrium, thus creating a field that drives electrons, the majority carrier, away from the interface. Consequently, holes are driven into the solution to perform oxidation. In a p-type semiconductor, the bands shift upward (more negative) to raise the Fermi level, creating a field that drives electrons into the solution. At the photocatalyst, photoelectrolysis is therefore a minority carrier driven process. On the counter electrode side, the metal has a much larger carrier density and is able to match the semiconductor Fermi level as it shifts. Upon illumination, the photogenerated charges counteract the electric field in the space charge layer, thereby flattening the bands to a degree dependant on the illumination intensity. With enough illumination, the semiconductor Fermi level will be at the flat band

potential, U_{fb}, which is the maximum (minimum in case of n-type) Fermi level possible without an external bias.

The n-type semiconductor Figure 6 a-d cannot split water without an external bias because the flat band potential of the semiconductor is below the hydrogen evolution potential. In (a), the metal Fermi level is aligned with that of the solution, but the semiconductor has not made contact with the electrolyte yet. In (b), the two electrodes are connected by a junction and both are in the electrolyte. The Fermi level of the semiconductor lines up with the electrolyte Fermi level. Due to band edge pinning, this causes the bulk bands to bend downward. In (c), the semiconductor is illuminated, creating photogenerated carriers that counteract the field in the space charge region, thus reducing band bending. Electrons that move through bulk to the metal still do not have enough energy for hydrogen evolution. Therefore, in (d), an external positive bias, E_b, is applied. As discussed before, the bias the distributed between both electrodes, thus lower the semiconductor Fermi level and raising the metal Fermi level. With enough bias, the electrons may reduce water. For a p-type semiconductor with U_{fb} too high, a negative bias is applied which raises the semiconductor Fermi level and lowers that for the metal. The ideal situation for a photoanode capable of self-driven water splitting is shown in (e).

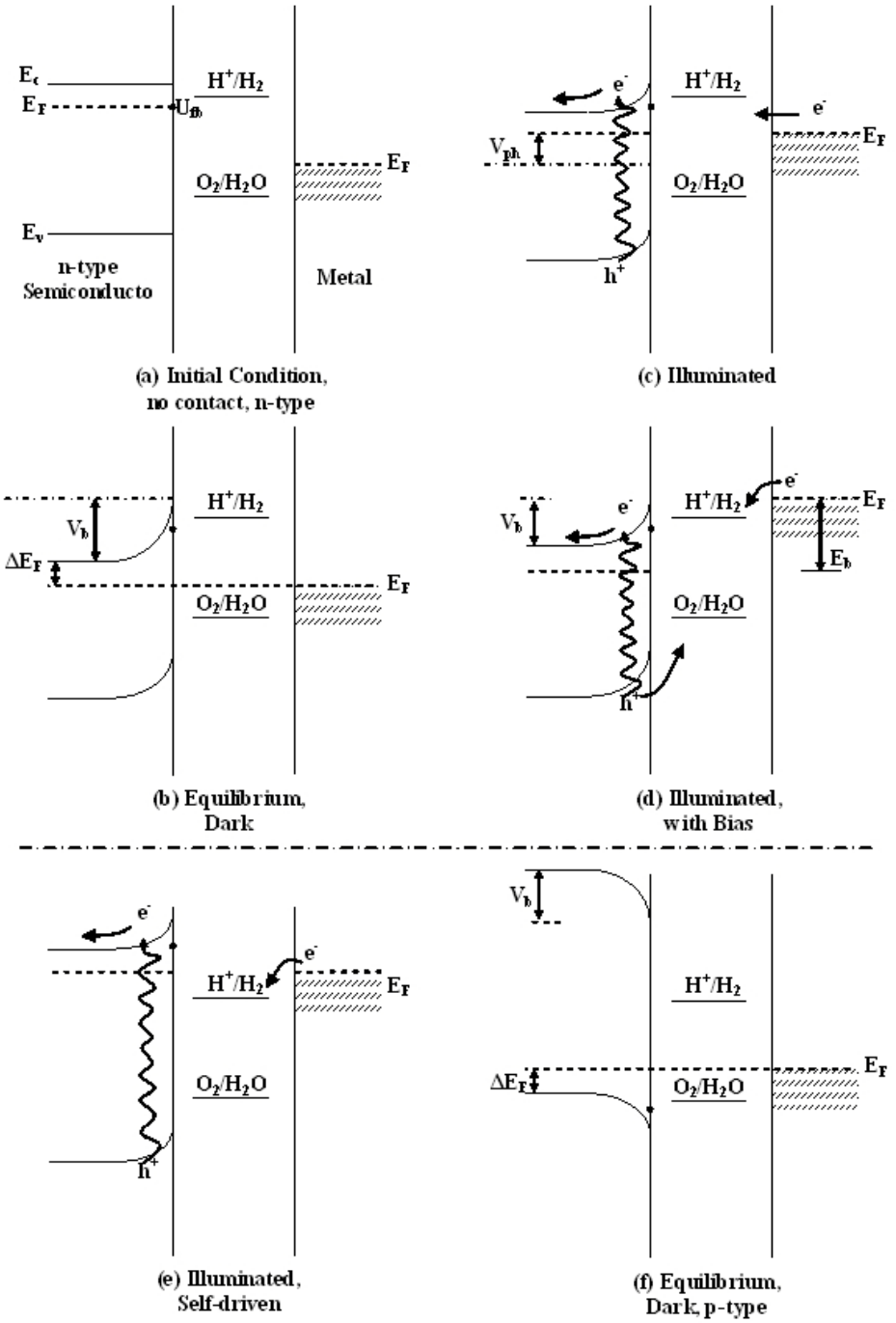

Figure 6. Energy level diagrams for n- and p-type semiconductors in electrolyte during photoelectrolysis. Figures (a) – (d) show the energy levels for an n-type semiconductor before contact with electrolyte or cathode, in equilibrium with the electrolyte and cathode in dark, with high intensity illumination, and with illumination and positive bias, respectively. In the latter figures, the semiconductor requires bias to perform photoelectrolysis, whereas the hypothetical n-type semiconductor in (e) does not need bias because its bands straddle the water splitting redox potentials. Figure (f) represents a p-type semiconductor at equilibrium in dark—correlating to (b).

PEC Material Requirements:

There are a number of challenges associated with searching for a suitable and stable material for performing photolysis. The criteria are[12]:

1) Band gap energy between 1.7 eV and 2.2 eV (roughly).

2) Appreciable reaction kinetics and charge carrier conductivity

3) The energies of the highest unoccupied and lowest occupied molecular orbitals "straddle" the redox potentials for water decomposition.

4) Stability in aqueous environments.

5) Earth-abundant, inexpensive, mass-producible

The minimum band gap requirement is dictated by the minimum energy needed to split water (1.23 eV), thermodynamic losses, and overpotentials needed to increase the reaction kinetics. The upper band gap requirement ensures that the semiconductor absorbs a significant portion of the terrestrial solar spectrum. It is not enough that the semiconductor absorb the photons, however, because it also must be able to separate and conduct the electrons and holes. As for stability, the semiconductor electrode may undergo corrosion. The third requirement refers to the relative energy band positions of the semiconductor. Essentially, the energy of the valence band should be greater than the water oxidation potential (1.23 eV vs. Normal Hydrogen Electrode) and the energy of the conduction band should be less than the water reduction potential (0 eV vs. NHE). The kinetics of charge transfer from the surface to the electrolyte must be faster than the decomposition reaction. For example, TiO_2 has excellent stability in a wide range of pH

levels whereas the corrosion of ZnO by oxidation is preferred over oxidation of water by the holes[13]. ZnO is stable as a photo-cathode (p-type), however, because the water reduction potential is greater than the reduction corrosion potential. Finally, the material cannot be composed of precious elements or else its application would be limited from the beginning due to economical impracticality. An expensive high-performance PEC system simply cannot be the solution. Similarly, there should exist, or be developed, a method for inexpensive mass-production in order to commercially feasible.

Efficiency

To date, the highest measured photoconversion efficiency for a photoelectrochemical cell is 12.4%, which was achieved at NREL using a $GaInP_2$/GaAs monolithic tandem cell[14]. That cell exhibited significant degradation, however. The photoconversion efficiency (STH)—also called solar to hydrogen conversion efficiency—is calculated using Equation (9)[15],

$$\varepsilon = \frac{1.229 I_P}{P_t} \tag{9}$$

where, the constant 1.229 is expressed in volts, I_p is photocurrent in A/m^2, and Pt is the input power (or light irradiance) in W/m^2. The constant comes from dividing the standard Gibbs energy for hydrogen evolution at 25 ºC and 1 bar (237.2 kJ/mol) by number of moles of electrons used to generate 1 mol of H_2 [4], and by the Faraday constant (96485 C). The numerator and denominator are both in terms of power units, and therefore efficiency is the ratio of power output to power input. This method assumes standard temperature and pressure conditions and that all the carriers are utilized

for evolving hydrogen and oxygen. The latter assumption is contradicted if the power output comes from photoelectrode corrosion. In order to use Eq. (9) to calculate efficiency, the photocurrent (current difference between dark and light conditions) must be generated without an external bias.

Although it is desirable for a photoelectrode to split water spontaneously upon illumination, some externally applied bias is most often necessary to encourage photocurrent. In such a case, Equation (9) must be modified as the following [15]:

$$\varepsilon = \frac{(1.229 - V_{bias})I_P}{P_t} \qquad (10)$$

where, V_{bias} is the externally applied potential. V_{bias} is the potential difference between the working electrode (photoelectrode) and the counter electrode. It is preferred to determine efficiency from two-electrode measurements. For three electrode measurements, V_{bias} is not measured by the potentiostat and must be determined with an external voltmeter.

Types of PEC Cells/Materials and Background Literature

The criteria for solar-driven PEC electrolysis are so selective that few semiconductors meet even the most basic requirements—band gap, band edge positions, and stability—though many semiconductors have been examined. There are different routes by which an ideal material may be found, such as by synthesizing a new semiconductor or by modifying those already studied. The possibilities for the composition of new semiconductors are practically unlimited when considering multi-elemental materials. Likewise, there are many options by which weaknesses of known

materials may be decreased or the strengths augmented. As such, this has been an active pursuit for many years and will continue to be so.

The most significant material types or strategies studied for solar-driven PEC may be classified according to three categories:

- Metal-oxide
- Group IV and III-V
- Other

There may also be some overlap among these categories both in terms of new materials and modifications. New materials are also being discovered—particularly those that are higher order than ternary combinations, but these will not be discussed because the reports are scarce.

Metal Oxide: The possibility of solar hydrogen production by solar-driven PEC electrolysis was first discovered with TiO_2 (titania) in 1972[16], and it has been studied continuously since then[17-29]. Titania is an attractive material for PEC because of its superb stability in aqueous environments with a wide range of pH levels. Furthermore, its band edges straddle the water reduction/oxidation potentials. As most oxides, it is a natural photoanode (n-type). The major issue with titania, however, is its large band gap ($E_g \approx 3$ eV), which limits the amount of solar energy it is capable of absorbing, significantly limiting the potential solar-to-hydrogen conversion efficiency. A large portion of the research has been directed toward reducing the band gap or maneuvering around the limitation. Attempts to decrease the band gap usually result in creating new problems, such as increased degradation. In fact, the natural stability of titania has been

attributed its large band gap, an indicator of the chemical bond strength[30]. Several other metal oxides have also shared much of the spotlight but failed to impress due to wide band gap. These include ZnO[31-33], WO_3[34-38], $SrTiO_3$ [39-42], $KTaO_3$, Ta_2O_5, ZrO_2 [11], and SnO_2 [43]. Some researchers have chosen an indirect route to enhancing the PEC behavior of some metal oxides by instead augmenting other properties, such as surface area. One method involves using one-dimensional morphologies, which will be discussed later in this chapter.

Iron oxide is an interesting and promising material for solar water splitting. There are three main types of iron oxides—FeO, Fe_2O_4 (magnetite), and Fe_2O_3 (hematite)—but it is hematite (α-Fe2O3) which exhibits the desired properties[44-85]. It is an n-type semiconductor with an ideal (though indirect) band gap of ≈ 2.2 eV, which means it can absorb a large portion of the terrestrial solar spectrum. Hematite has also been shown to exhibit good stability over a wide pH range (pH > 3). It is particularly appealing because it is cheap, relatively easy to synthesize, environmentally benign, and composed of two of the most abundant elements on Earth. Hematite has had limited success as a PEC material for several reasons, however. As a pure-phase material, it is a known Mott-insulator, which means that, though charge separation occurs, charge transport properties are poor[68, 75, 81]; typically synthesized as low quality polycrystalline films, it exhibits high recombination rates due to crystal grain boundaries and unordered oxygen vacancies[86]; it exhibits anisotropic conductivity, wherein conductivity along the (001) plane is four orders of magnitude higher than in the [001] direction[45, 55, 81], which is again an issue for polycrystalline films; and the conduction band edge is typically ~0.2 eV too positive for unbiased hydrogen evolution[87]. It has been suggested that these

issues may be solved by inexpensive means of modifying the material. Several studies have shown significant improvements through doping/alloying—Ti[49, 51, 79], Si[47, 49, 56, 60], Pt[50], Ge[60], Mg[52, 72, 88], Zn[54, 65, 89, 90], Ta[91], Nb[87, 92], Cr, Mo[64], Cu[53], and Al-Ti[93]—and surface modification—Co[56], and Fluorine[51]. Of the studies, the most significant improvements have been attained by introducing Ti and Si, which increase the conductivity due to increased donor concentrations and, in the case of Si, improves crystallinity, reduces crystal size, and influences orientation of the (001) basal plane. As for surface modification, cobalt improves water oxidation catalysis and fluorine is claimed to lower the energy of the conduction band edge. Manipulating structural characteristics such as morphology and improving crystallinity may also reduce or eliminate the limitations, which is the focus of this study. Some positive results have already been shown with the use of nanorod structures, which are discussed in more detail later.

Several different methods have been developed for synthesizing hematite samples: single crystal synthesis[94, 95], ceramic processing[91], sol-gel[96-100], physical vapor deposition[101], chemical vapor deposition (CVD) [28, 56, 68, 71, 102], direct plasma oxidation[103-105], aqueous self-assembly[44, 106], electrochemical deposition[50, 64, 107-109], direct thermal oxidation [110-112], and spray pyrolysis[52, 53, 66, 89, 93]. The later is probably is most popular method among photoelectrochemical studies because it allows for easy introduction of precursors containing foreign impurities. Most of these methods produce polycrystalline films which have their own set inadvertent disadvantages, as discussed before, while some others are impractical for large scale synthesis. Both thermal oxidation and plasma-

assisted have been shown to reproducibly grow high quality nanostructures of hematite. Direct plasma oxidation, however, is quicker and may have other advantages, which this study attempts to show.

Group IV and III-V: There are many possible binary, ternary, and quaternary combinations of group III-V and IV elements that yield semiconductors with interesting properties. The advantage of these materials is that they are typically synthesized as high purity single crystal films using metal organic CVD, yielding high efficiencies. For PEC applications, the fatal flaw of these materials is poor stability and band edge mismatch. All binary III-V materials are aligned to drive the hydrogen evolution reaction, but only GaN is capable of evolving oxygen[113, 114]. GaN has a too wide band gap (3.4 eV), however. SiC, a binary group IV semiconductor, shares a similar fate. It is well aligned for water splitting and is stable against corrosion, but it too has an unacceptably wide band gap (3 eV)[115]. Furthermore, the high purity of these materials requires exuberantly expensive equipment and processing.

Elements from groups III and V may be combined in ternary, quaternary materials, and even higher order materials to yield interesting properties. Often, the intent is to find a happy medium between the properties of two or more semiconductors. For example, combining InN (0.7 eV) with GaN yields a InGaN with varying compositions and likewise varying band gaps (between those of InN and GaN)[116-119]. Other such materials studied for PEC applications include $GaInP_2$ [120-122], GaAsPN, GaPN, and GaInPN[123, 124]. GaAsPN exhibited high corrosion while $GaP_{0.98}N_{0.02}$ was found to have a band gap of 2 eV, but the introduction of N caused lattice mismatches between the underlying GaP layer and significantly reduced the efficiency. At the same

time, minute nitrogen concentrations were shown to reduce vulnerability of the material to corrosion. By using indium in $Ga_{.962}In_{.038}P_{.976}N_{.024}$ and $Ga_{.95}In_{.05}P_{.975}N_{.025}$, lattice mismatching was solved and these materials also had a direct band gap of 2 eV, but still exhibited low efficiencies.

A tandem cell is a combination of two or more semiconductor materials connected by ohmic contacts. These are stacked such that wider band gap materials are nearer to the illumination source, allowing the lower energy light to pass through to the next material. This way, more photons may be absorbed and higher efficiencies may be attained. Tandem cells may overcome the energetic mismatch of the III-V matrials. The highest solar-to-hydrogen efficiency PEC cell is a tandem cell using p-GaInP2 on a p/n GaAs junction, which is the 12.4 % cell mentioned in the previous section[14]. The excited electron from the top p-GaInP2 layer reduces hydrogen while its hole combined with an excited electron from the GaAs layer. The hole left in the GaAs then proceeds to the metal cathode to drive the oxidation process. Of course, the problem of stability and cost still remains.

Other: Many other materials and strategies have been employed for PEC applications. Metal sulfides (e.g. MoS_2), particle suspensions, protective coatings, and hybrid architectures, just to name a few. None have thus far come close to addressing even a majority of the requirements for successful water splitting application, although each are significant pursuits. For more thorough discussions of these and other developments, the reader is referred to the following review articles: [11, 12, 23, 26, 125, 126].

Nanowires for PEC

One example of a modification to an existing material to improve PEC performance is morphology. In this regard, the use of nanowires can be advantageous. Nanowires offer a high surface-to-volume ratio, which means that using nanowires rather than a flat surface increases the reaction surface area leading to greater current. Nanowires can have fewer (or no) grain boundaries[44, 103, 104], which are a serious problem in polycrystalline films because they act as electron-hole trap sites[46]. Furthermore, nanowires are an excellent platform for doping and alloying studies. One way to increase the STH efficiency of hematite, for example, is to minimize the distance through which the minority carriers must diffuse, thus reducing the probability of recombination losses[67]. The geometry of nanorods/nanowires achieves just this, and in addition the perpendicular orientation better facilitates charge transport to the back contact without loss due to random pathways such as in nanoparticle systems. Reducing the feature size, to sub 5 nm dimensions may lead to quantum confinement[127], which may actually be beneficial if it leads to a decrease (upward shift) in the conduction band energy without a significant increase in the total band gap. 1-D nanostructures are relatively new in this field, but several studies have already demonstrated that they perform better than particles or thin-films.

Several groups synthesized TiO_2 nanowires and nanotubes and demonstrated improved performance compared to films or particles[22, 24, 25]. One study in particular found that the nanowires achieve a two-fold increase in photoconversion efficiency over a single-layer film[22], and another study demonstrated a twenty-fold increase in photocurrent over a nanoparticulate film[24]. These studies have attributed the increased

activity to increased surface area and reduced grain boundaries. These observations are not limited to TiO_2, however. Other materials, such as hematite—as discussed above—and ZnO have been shown to benefit from 1-D geometries for photoelectrochemical water-splitting. An array of ZnO nanorods exhibited a photocurrent twice that of a ZnO thin film in the same study[33].

Synthesis of hematite nanowire or nanorod architectures has been demonstrated using different methods[102-104, 110, 111, 127-132]. Using pure oxygen RF plasma, nanowire arrays of several oxides were synthesized in a matter of seconds[103]. Subsequent studies of showed that the hematite nanowires were single-crystalline and exhibited a superstructure of repeating oxygen vacancy planes parallel to the growth direction along the (001) basal plane[104, 105]. As mentioned earlier, hematite exhibits higher conductivity along the (001) plane, which means that these nanowires may exhibit excellent charge carrier conductivity to the back contact. Oxygen vacancies in hematite are traditionally responsible for significant losses in charge carrier conductivity, so the potential advantage of these nanowires for PEC electrolysis is that the carriers may conduct to back contact without encountering vacancy trap sites. Discoveries such as these continuously demonstrate the benefits of nanowire architectures for PEC electrolysis.

Purpose and Intent of this Study

This study reports different methods for synthesizing hematite nanostructures, with a focus on nanowires, and their respective performance for PEC water splitting.

Primarily, this compares PEC performance of hematite electrodes produced by direct thermal oxidation and plasma oxidation methods, two of more promising and scalable methods.

II. INSTRUMENTATION AND EQUIPMENT:

The section includes descriptions of the tools, equipment, and methods used in the study. Experimental conditions and parameters will be described in section III.

For synthesis:

- Atmospheric microwave plasma (AMWP) jet reactor
- Ambient furnace oven

For characterization and analysis:

- Photoelectrochemistry (PEC) setup
- Scanning electron microscope (SEM)
- Electron diffraction spectroscopy (EDS)
- Raman and photoluminescence (PL)
- Transmission electron microscope (TEM)
- Ultra high vacuum (UHV) system equipped with ultraviolet photoelectron spectroscopy (UPS) and x-ray photoelectron spectroscopy (XPS)
- UV-Vis
- X-Ray diffraction (XRD)

Atmospheric Microwave Plasma Jet Reactor

Plasma oxidation was performed using an in-house designed and assembled microwave plasma reactor fitted with a vertical 1.5” diameter quartz tube[133]. A delivery chuck at the top allowed for gases to be introduced in a concentric fashion to

serve both as a cooling sheath for the tube to keep the reacting powder in the center. The reactor can operate at a pressure range of a few torr and powers of 300 W to 3 kW. The sustained plasma jet ranged was 12 to 15 in. The schematic is shown in Figure 7.

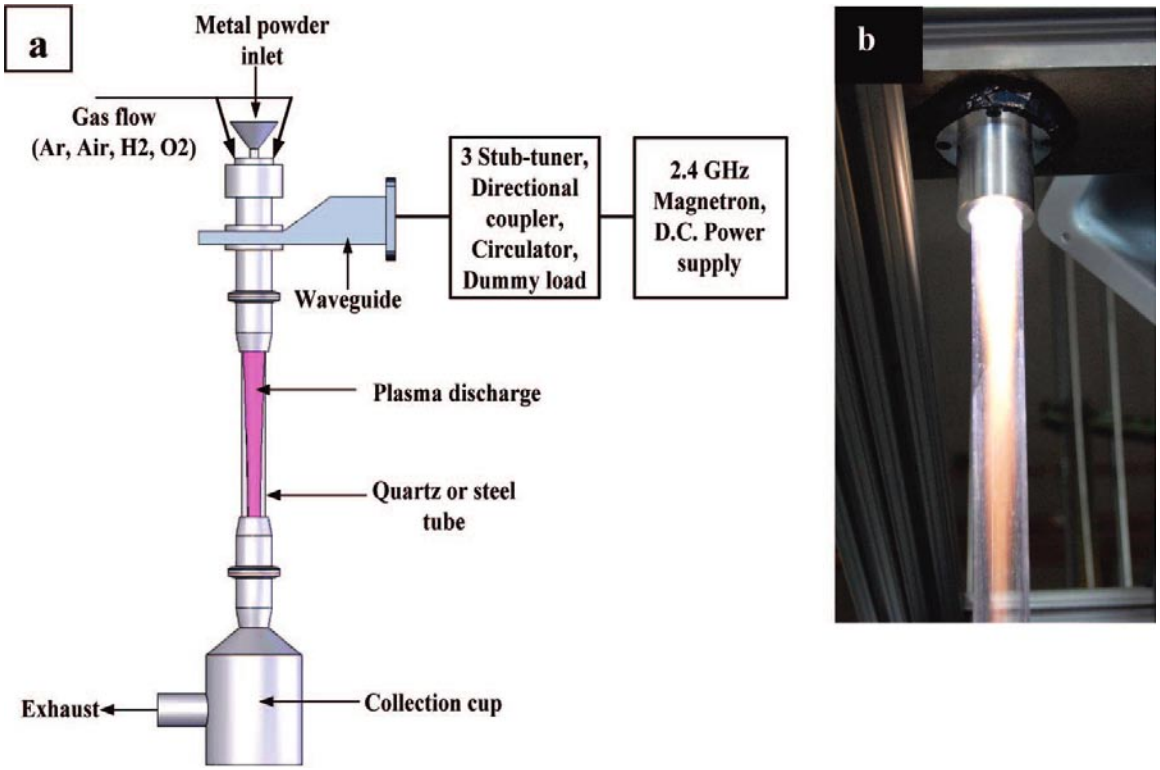

Figure 7. Microwave plasma reactor designed to create a plasma jet at atmospheric conditions. Metal powders fed from the top form metal oxide nanowires collected at the bottom[133].

Ambient Furnace Oven

Thermal oxidation synthesis was performed in a Barnstead Thermolyne 1400 FurnaceIt is capable of operating at temperature ranging from room to 1000 °C.

Photoelectrochemistry Setup

The PEC test instrumentation include:

- Princeton Applied Research Model 273A Potentiostat/Galvanostat
- Three-electrode cell glass cell with a quartz front window.
- Oriel 300W Xe lamp solar simulator from Newport Instruments
- Newport model 77330 monochromator
- Thorlabs D10MM power meter with model PM100 readout
- Computer with PowerSuite electrochemistry software
- Glass cell with a quartz window and two compartments separated by a porous glass frit
- Platinum mesh counter electrode
- Several different reference electrodes were used
    - Ag/AgCl, MF-2052 from Bioanalytical Systems, Corp
    - Standard Calomel Electrode (SCE), Accument 13-620-51
- Ultra High Purity N2 line for sparging

The glass cell has two compartments to isolate the WE and CE so that the evolved O2 and H2 may be collected separately. In this study, only the electrochemical data was analyzed for performance evaluation. Therefore, all three electrodes (WE, CE, RE) were placed in a single compartment to eliminate any contribution to resistance to ion flow by the glass frit. A typical setup is shown in Figure 8.

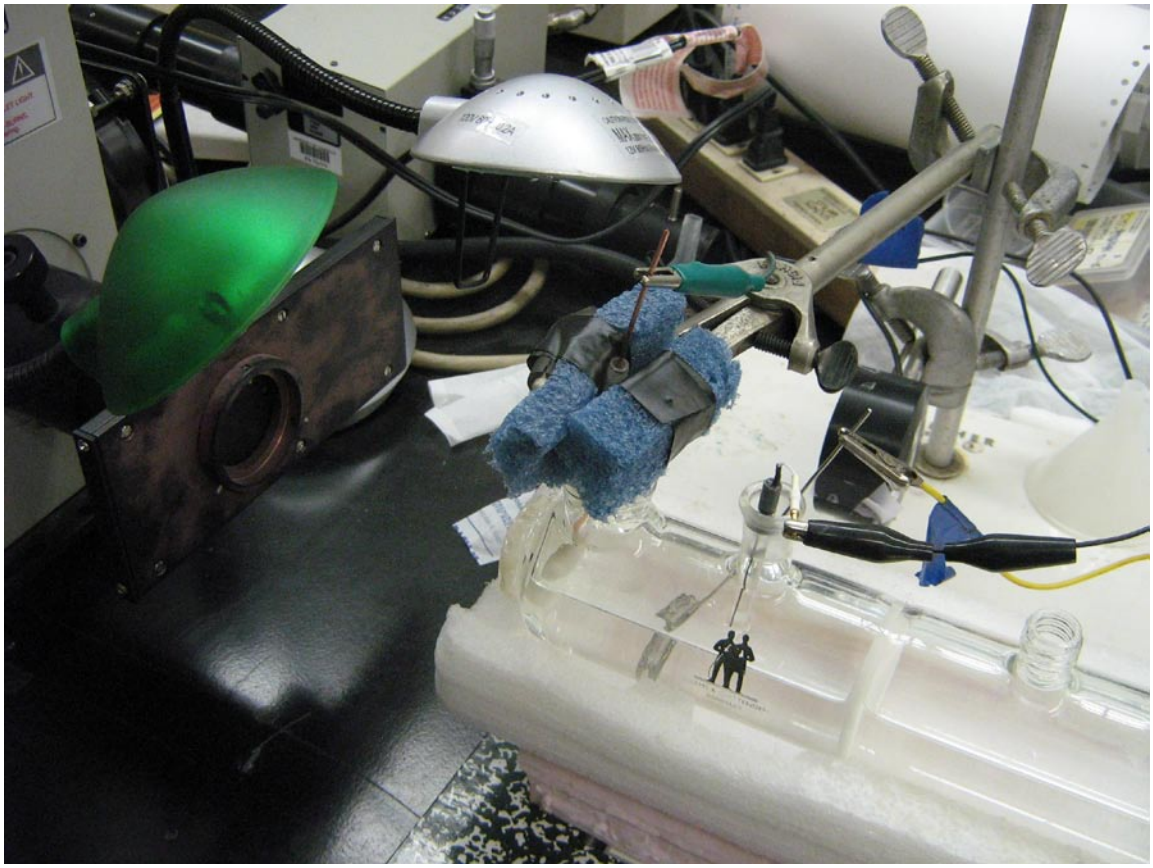

Figure 8. Photograph of a PEC cell with a three-electrode setup in front of a light source.

Scanning Electron Microscope

An SEM is a surface analysis technique particularly useful for topographical and morphological assessment. An FEI Nova 600 NanoLab SEM was used to analyze the synthesized samples. It uses a field emission gun to generate an electron beam which is focused with electromagnetic lenses and apertures onto the sample. Scanning coils then raster the beam across the sample. Interaction of the beam with the sample emits Auger electrons, X-rays, backscattered electrons, cathodoluminescence, and secondary electrons. Backscattered electrons are the result of elastic interaction, in which case energy is conserved, while the other emissions are inelastic interactions. Secondary

electrons, which are emitted after the primary electron (incident beam) are absorbed, are typically used for surface topography imaging. An "In-Lens Detector" was used to collect only the secondary electrons.

EDS

Electron diffraction spectroscopy (EDS) is used to analyze elemental composition. A detector collects the X-ray emission resulting from the electron beam and sample interaction in an SEM. Each element has a unique core shell structure, which results in unique X-ray signals. A commercial system from EDAX was used for the EDS. The instrument was setup in a JEOL 5310 SEM with Li thermionic emission source.

Raman and Photoluminescence

Raman is a technique primarily used to evaluate the phase of materials, as well to confirm the composition. A focused monochromated infrared laser interacts with the sample, resulting in inelastic scattering which is collected by a detector. There is a material phase-specific change in the energy of the scattered photons from the source laser, which is known as the Raman shift. Photoluminescence is a similar technique performed in the same instrument, but it uses a high energy UV laser to determine the energy band structure of a material. The band gap and defect states within it may be detected. A Renishaw Invia Micro Raman system was used. It has He-Cd (325 nm) and Nd-YaG (633 mn) lasers for the PL and Raman analysis, respectively. The resolution of the Raman spectroscopy in this setup is 1 micron.

UPS

Ultra violet photoelectron spectroscopy (UPS) is a surface study techniques. It involves exposing a sample to UV light, which causes excitation of valence electrons. It is used to analyze the valence band structure, and particularly the Fermi level energy, conductivity type, of a semiconductor, and work function. This technique is highly sensitive to the top few nanometers, making it an excellent technique for study a material surface, adsorbates, and functional groups. The analysis is performed under highly controlled ultra-high vacuum conditions. A VG Scientific / RHK 62 Technology multi chamber UHV surface science system was used, with a 150 mm radius CLAM 4 hemispherical analyzer. A differentially pumped He-discharge lamp was used to generate UV radiation.

UV-Vis

UV-Vis spectroscopy is a versatile tool for studying optical properties of materials. Absorbance, transmission, or reflectance data are collected, from which one can determine the band gap value and type (in/direct) of semiconductors, among other valuable information. For solutions, this technique can also be used to determine the concentration of solutes. Light impinging on a sample is absorbed, transmitted, or reflected. The degree to which each of these happens depends on the particular material of interest. Performing calculations and analysis will be discussed in the Results section.

A UV-Vis spectrometer uses multiple light sources (tungsten filament for visible region and deuterium lamp for ultraviolet region), a grating to monochromate the light, and a photodiode or CCD detector. For solutions, the monochromated beam is split into

two by a half-mirror after which one beam goes through the reference solution (usually pure solvent) and another goes through the sample. The transmitted light is then collected by the detector and the software calculates the absorbance/transmittance values. Diffuse reflectance measurements are performed for opaque solid samples using a diffuse reflectance integrating sphere. The sphere has ports for the incident beam, the sample, and the detector. A plug is positioned at an appropriate angle to absorb the specular reflectance—only diffuse reflectance should be collected for the measurement. The shape of the sphere channels the diffuse reflectance to the detector port. A highly reflective standard (typically Ba_2SO_4 or PTFE) is used as a backing for a sample so that any transmitted light is reflected back. A Perkin Elmer Lambda 950 UV-Vis spectrometer was used in this study.

III. PROCEDURE/EXPERIMENTAL METHODS

RF Plasma Oxidation

Commercial iron sheets (98%) 3mm thick were exposed to an O-rich RF glow discharge plasma at low pressure (100 Pa) for 90 seconds. The process is described in detail in several publications[103, 104, 128, 134].

Atmospheric MW Plasma

Iron sheets (99.5 %, from Advent Research Materials) 2 mm thick were cut into one square centimeter pieces. The pieces were then sanded down (220 grit) to remove any native oxide or surface contamination, cleaned with ethanol, and promptly dried with Kim Wipes. An atmospheric plasma jet reactor, described elsewhere[133], was used to generate a plasma consisting of air, argon, and oxygen. The setup was modified for this synthesis method such that the plasma flame was directed upwards. The flow rates varied but were usually about 15 lpm, 2 lpm, and 500 sccm, respectively. The iron pieces were then exposed in the plasma jet. The iron pieces were held in the plasma flame with tweezers about 3” from the base. Exposure time varied from a couple to twenty minutes.

Ambient Oven Oxidation

Iron sheets (same as above) were spaced out on aluminum foil, pressed down to ensure good contact, and placed in a furnace oven pre-heated at 500 °C. Although 5 hours was enough to grow a layer of nanowires, ribbons, flakes, and belts, the samples were held in the oven for 12 hours.

Atmospheric Plasma Torch Powder

The atmospheric plasma jet reactor shown in Figure 7 was used with a (≈ 10") plasma consisting of 12.45 lpm of air, 2 lpm of Ar, 300 sccm of H2, and 500 sccm of O2. A pump was used to draw the gas (and plasma) downward. Iron powder (<10 μm, Sigma Aldrich) was slowly poured from the top. The powder reacted as it fell through the plasma by gravity. Products were collected in a cup placed directly below and from a filter (1 μm) placed in the way of the exhaust.

Electrodeposition of Fe Thin Films and Pt Surface Catalyst

Electrodeposition on Fe onto conducting substrates (e.g., glass slides coated with fluorine doped tin oxide, or FTO) was performed using the same electrochemistry instrumentation as for the PEC setup described in the previous chapter. Using references [135, 136] as examples, an electrolyte solution was prepared containing: 0.075 M H_2SO_4, 0.9 M $FeSO_4 \cdot 7H_2O$, and 0.15 M $FeCl_3 \cdot 4H_2O$. Before any set of experiments, the solution was sparged with high purity N_2 for approximately 10 minutes. The electrodes were then submerged in the solution, with the WE lead connected to the substrate (FTO), the CE lead connected to an Fe foil (99.5%, 0.025 mm, Alfa Aesar), and the RE shorted with the CE. The solution was constantly agitated during deposition using a magnetic stir rod. The PowerSuite software was used to setup a Galvanic Square Wave experiment wherein the appropriate current was pulsed for one second and then zero current for one second, repeated. The current pulse was calculated based on the substrate area, desired film thickness, and desired time of experiment. For example, with an immersed FTO area of 9.1 cm^2 and a desired film thickness of $1 \cdot 10^{-4}$ cm (1 μm), the total volume of Fe is $9.1 \cdot 10^{-4}$ cm^3, corresponding to $1.3 \cdot 10^{-4}$ moles (ρ = 7.874 g/cm^3, MW = 55.845 g/mol), or 12.4 C

(F = 96485.34 C/mol). For a twenty minute experiment (total time), the current pulse needed to be 20.6 mA (12.4 C / 600 sec).

In some cases, minute amounts of platinum were electroplated onto the semiconductor electrodes to enhance catalysis of the oxidation reaction. As above, a two electrode setup was used. The electrolyte was Platinum AP RTU solution from Technic Inc. A galvanic square wave function was used, wherein current was applied for 0.25 seconds and zero current was applied for 2 seconds. The cycle was repeated until 10 mC/cm^2 was achieved.

Electrode Preparation

For PEC characterization, it necessary to have only the semiconductor surface exposed to the electrolyte and to have a low-resistance ohmic contact. The following procedures were applied for Fe_2O_3 films on 1 cm^2 iron substrates: 1) the oxide on one side was sanded down until only the metallic shine of iron was exposed; 2) a copper wire was coiled at one end to an approximate diameter of 1 cm2, and then one side of the coil was sanded down to remove native oxide; 3) after spreading silver epoxy (CircuitWorks two-part conductive epoxy) on the sanded side of the copper coil and on the sanded side of the sample, the sample was pressed onto the copper; 4) the assembly was then held in an oven heated to 80 – 120 °C for about 20 minutes to cure the epoxy; 5) the assembly was then inserted into glass tubing (copper tail first), such that some of the copper wire sticks out at the end and the other side of the glass tubing is touching the coil/sample; 6) a thick layer of Hysol 9462 epoxy was spread onto the sample area of the assembly such that everything except the Fe2O3 surface was insulated; 7) this assembly was put into the oven at 80 C for approximately 2 hours, or until the epoxy was hard; 8) a thin layer of

Hysol E-120HP was then spread over the previous epoxy layer; 9) this assembly was then put into the oven at 80 C, or until the epoxy was cured; 10) before performing any tests, the tail end of the copper wire was sanded down to remove any oxide that developed while in the oven. Figure 9 shows the electrode at different points in the above procedures. Hysol 9462 may be used alone, but Hysol E-120HP was added for extra protection against corrosion.

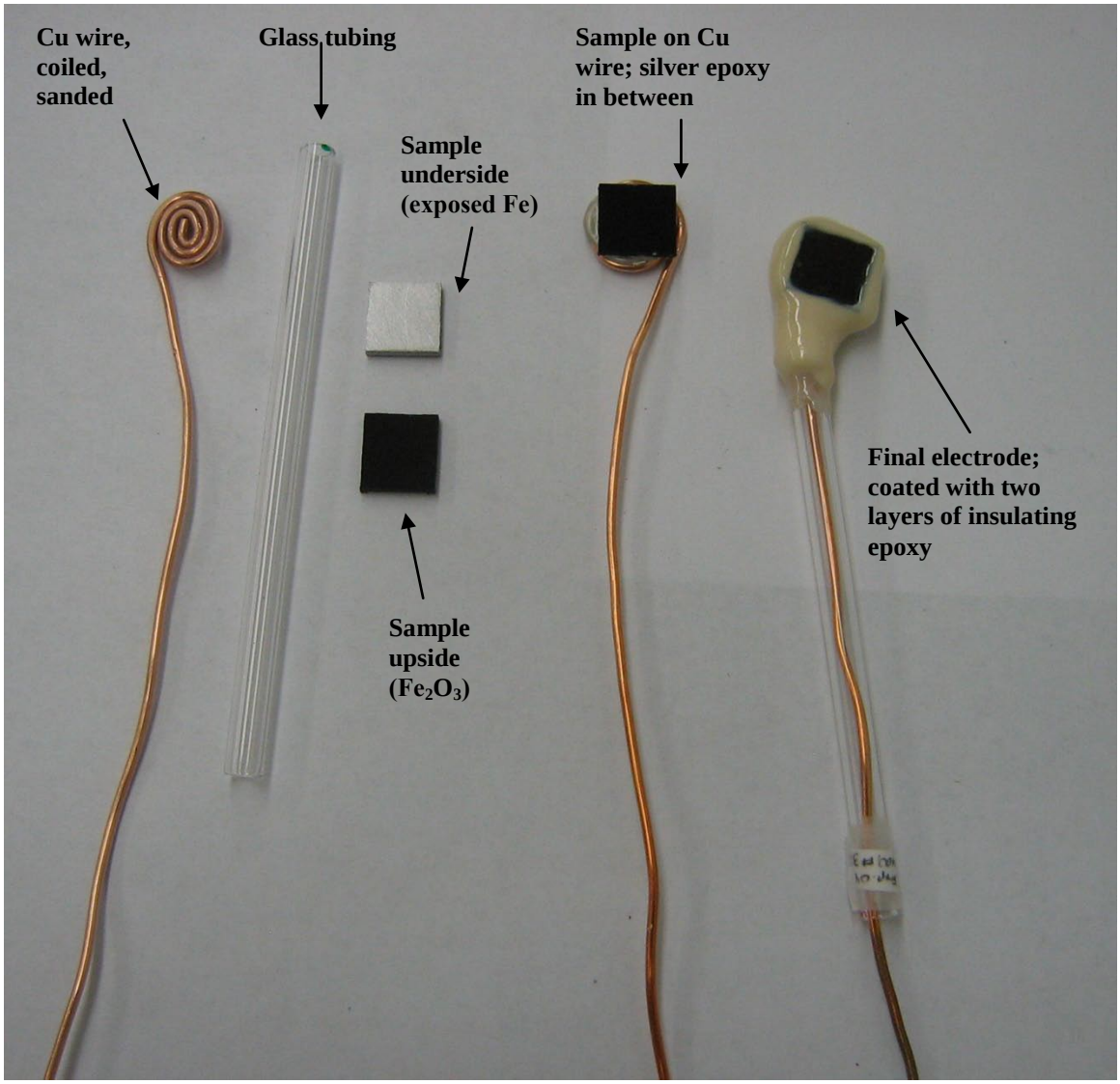

Figure 9. A picture showing the different steps of making a typical electrode.

Some samples in this study required slight modifications to the above procedures. For samples on FTO (Hartford Glass, TEC 8) glass, the oxide film was only in the center and the outer edges were covered with conducting silver epoxy. Then, copper wire was placed in good contact with the silver epoxy and the assembly was cured, following by coating with the insulating epoxies. Figure 10 shows a typical FTO electrode before and after coating with insulating epoxy.

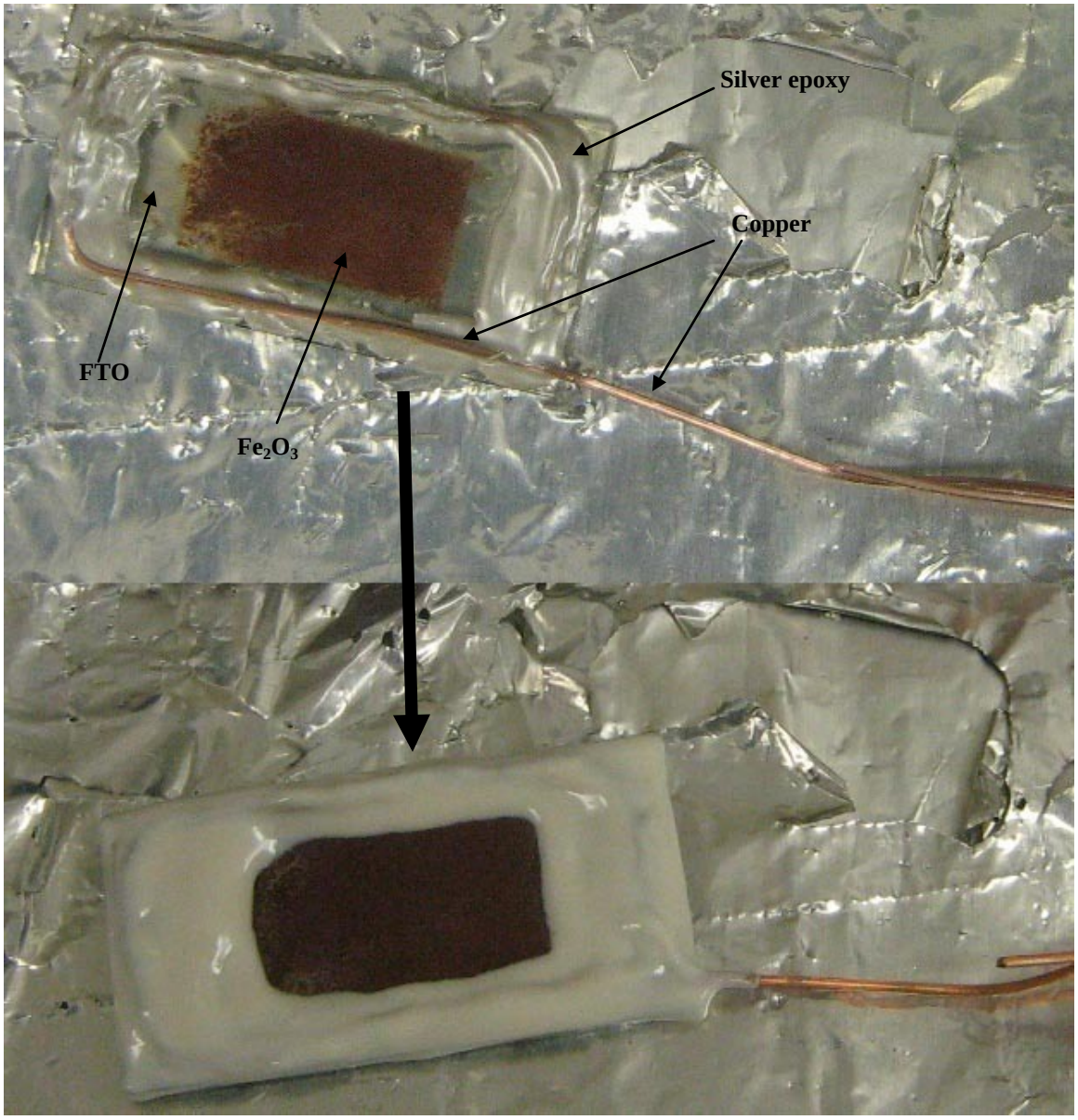

Figure 10. FTO electrodes showing how conducting contact was made. The bottom image was taken after coating the electrode shown at the top with insulating epoxies.

The final procedure was to calculate the geometric surface area of the semiconductor surface area. Using a copy machine, the electrodes were copied with printed, oxide side down, with 200% magnification. The image colors were inverted such that the oxide part of the image printed out as solid white while the rest was dark. Then, grid paper was also copied with 200% magnification. A square was cut out of the

copied grid paper corresponding to 1 cm^2 on the original, and weighed. Then, the semiconductor area of the copied samples was cut out and also weighed. The surface area was then determined using the following Equation (11):

$$\frac{sample\ \ cut-out\ \ mass}{1\ cm^2\ \ grid\ \ mass} x1cm^2 = sample\ area \qquad 11$$

Photoelectrochemistry

Open Circuit Potential (OCP): As discussed in the theory section, the bands within a semiconductor will flatten out upon illumination. Bending occurs in opposite direction for n-type and p-type semiconductors. Measuring the potential of a semiconductor in an open circuit before and after illumination will therefore reveal its conductivity type. This test is called OCP. A positive potential shift upon illumination indicates p-type conductivity. OCP measurements were performed using a three-electrode setup in 1 M KOH solution with AM 1.5 (100 mW/cm^2) illumination. Acidic solution proved to be corrosive for the samples. In order for the potential readings to reach equilibrium, OCP was typically performed for a duration of about 180 seconds, with light being turned on at 90 seconds.

Current Density-Voltage (J-V): J-V tests may be performed in a two or three electrode setup. Potential is applied to the sample at a specified scan rate within a specified potential window, and the current is measured. In this study, the scan rate was 25 mV/s and the solution was 1 M KOH. These tests may reveal a myriad of information about the material and its behavior under PEC conditions. Two electrode tests are run to determine the STH and three-electrode measurements are used to characterize energetics and kinetics at the semiconductor. J-V scans are run in dark and subsequently in light,

and the photocurrent is determined by the absolute value of the difference. Samples are normally biased in the positive direction for n-type samples and in the negative direction for p-type samples. A typical dark/light J-V scan for an n-type semiconductor may look as shown in Figure 11. Inversion occurs when enough bias applied to band the bends such that the Fermi level is in the valence band at the surface, in which case the surface is flooded with holes and the semiconductor exhibits metallic conductivity. Operating in this region may lead to corrosion of the material. The dark current onset potential corresponds to the onset of inversion. The photocurrent onset correlates to the potential at which the band edges the charge carriers are energetic enough to drive the redox reactions. Refer to Figure 6 for band energetics diagrams.

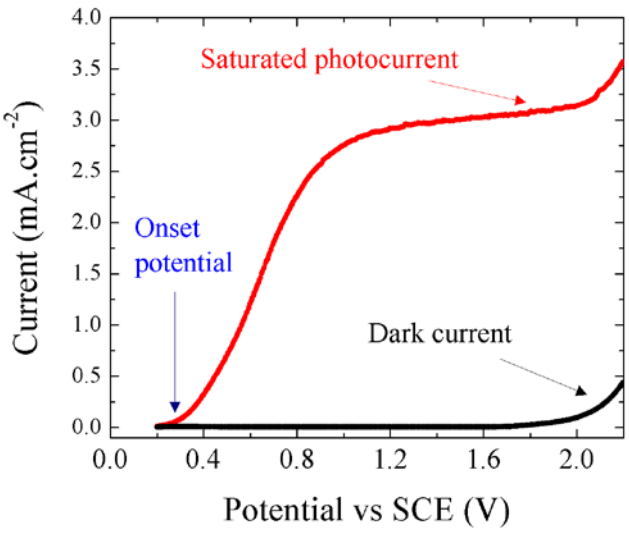

Figure 11. A typical dark and light J-V scan for an n-type semiconductor.

UPS

Gold was sputtered on about a third of the surface of each sample for reference and calibration. The instrument has a work function of 4.5, which cause the low kinetic

energy (KE) peaks of the samples to be hidden. Therefore, a battery was used to apply a bias greater than 4.5 V to the sample. The tests reported used three different bias values, 5.68, 5.81, and 7.40 V.

IV. RESULTS AND DISCUSSION

This study involved synthesis, structural characterization, and PEC properties and performance analysis of each sample. Also, different types of samples were synthesized and tested. This section will therefore present and discuss findings in the above order.

Synthesis

Figure 12 presents SEM images of the results of direct plasma oxidation of iron substrates by RF oxygen plasma and of NPs grown by plasma oxidation of iron powder. The NWs (a) are approximately 100-200 nm at the base and are one to three microns long, and cover the most of the iron substrate surface. The NPs aggregated into large clumps, but individually vary in size from 10 to 100 nm.

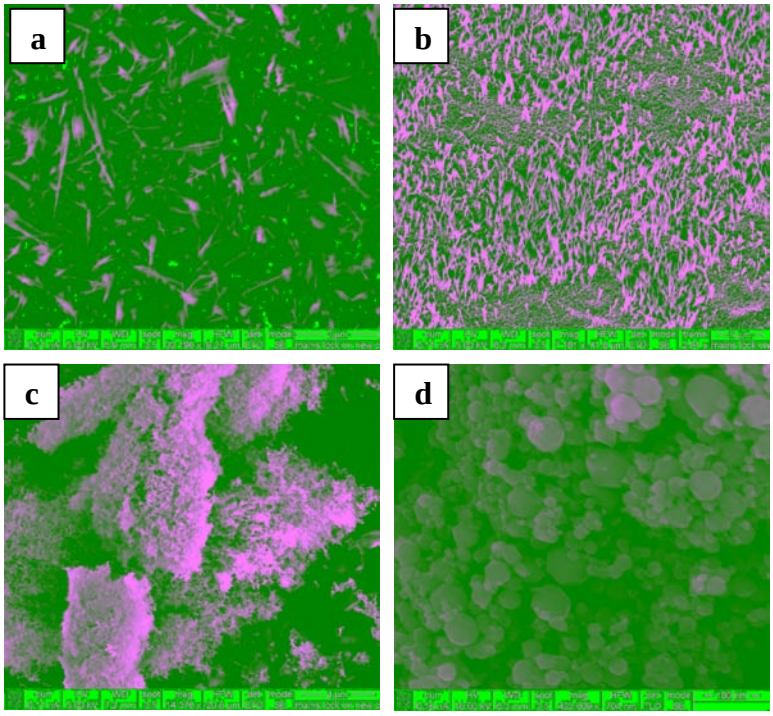

Figure 12. SEM images of hematite (a) NWs grown by direct plasma oxidation of iron and (c,d) NPs also grown by plasma oxidation.

Thermal oxidation of Fe sheets was performed at three different temperatures: 500 °C, 600 °C, and 800 °C. These temperatures were chosen to encompass and exceed the Fe-O transition temperature for α-Fe_2O_3 (570-580 °C) [MIT database] and because previous studies suggested that this is an appropriate range[111]. At 500 °C, three types of morphologies were observed: nanowires, nanoflakes, and larger wave-like nanoribbons. The nanowires were visible when looking at a curved surface or when tilting the sample. The nanowires occurred in dense arrays and were on the order of 5 μm in length and tapered—from 100 nm to 10 nm, roughly. The nanoflakes uniformly covered the entire surface. Their dimensions were roughly 1 μm at the widest point and tens of nanometers thick, though that was difficult to measure from SEM images. The nanoribbons—typically a few μm tall, tens of nanometers thick, and extending out for several μm—sometimes occurred in small or large batches but usually they were uniform throughout. All three morphologies existed in the same locations, densely packed together. The results for 600 °C were less consistent, yielding either only nanowire arrays or a combination of nanowires and nanoflakes, but never nanoribbons. Figure 13 shows SEM images of the thermal oxidation results, except for samples oxidized at 800 ºC. In the latter case, the samples lacked the distinct rust color of hematite and SEM images revealed an amorphous top layer. This indicates that a molten layer existed which then solidified without forming nuclei for nanowire (or other morphology) growth. All subsequently tested on thermally oxidized samples were grown at 500 C.

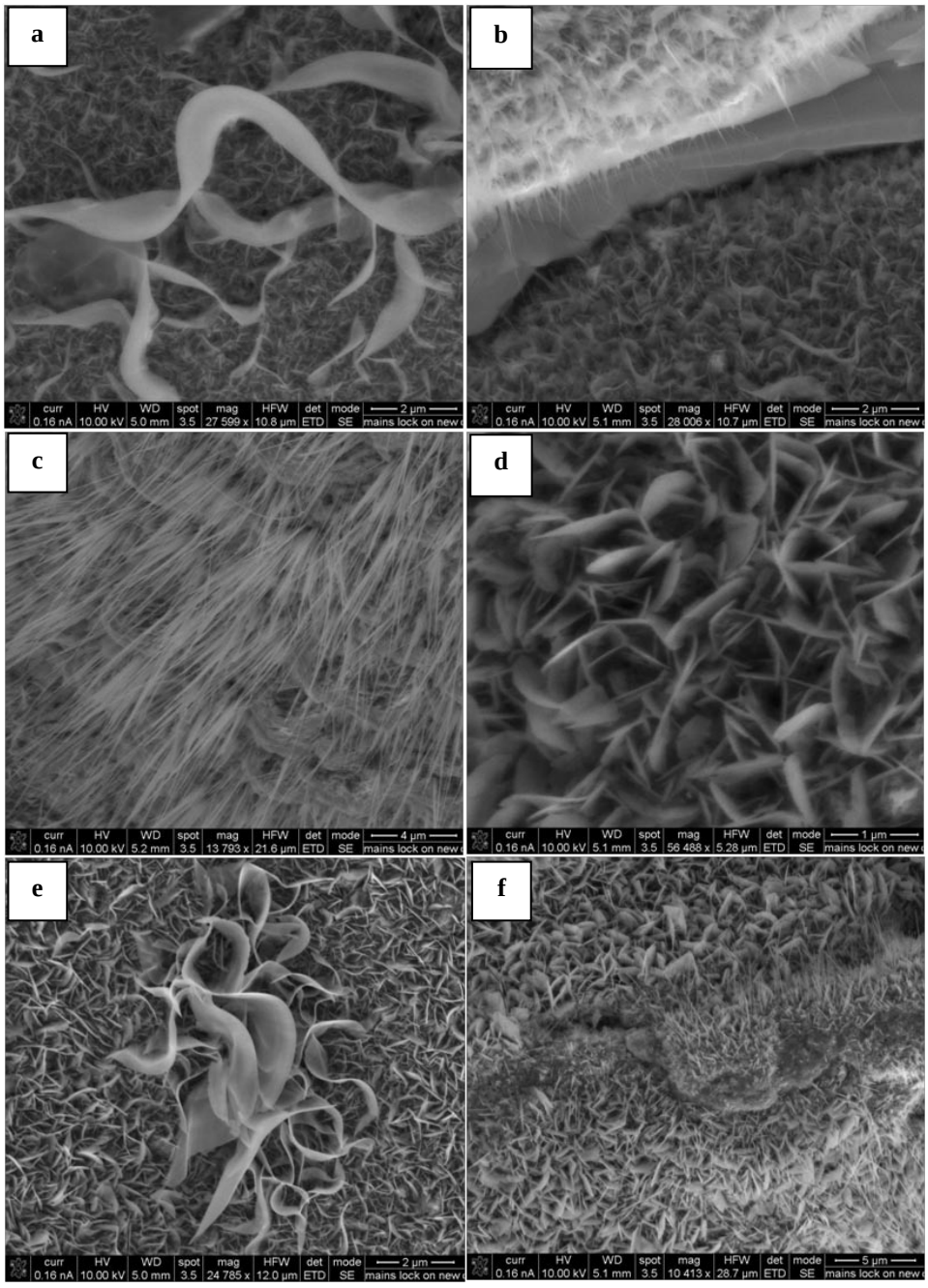

Figure 13. SEM images of thermally oxidized Fe sheets at (a-b, e) 500 °C and (c-d, f) 600 °C. Flakes and wires grew in all experiments, but larger ribbons were observed only at 500 C. Oxidation at 800 C (not shown) resulted in an amorphous surface layer.

Characterization

Raman

Raman was performed on NWs grown by O_2 plasma treatment. The Raman peaks, shown in Figure 14, agree well with those reported earlier[104, 111, 137], confirming the α-Fe_2O_3 phase. Most of the peaks for thermally oxidized samples are slightly shifted positive from those of the plasma oxidized. This may be due to laser heating, however, because a higher intensity was used.

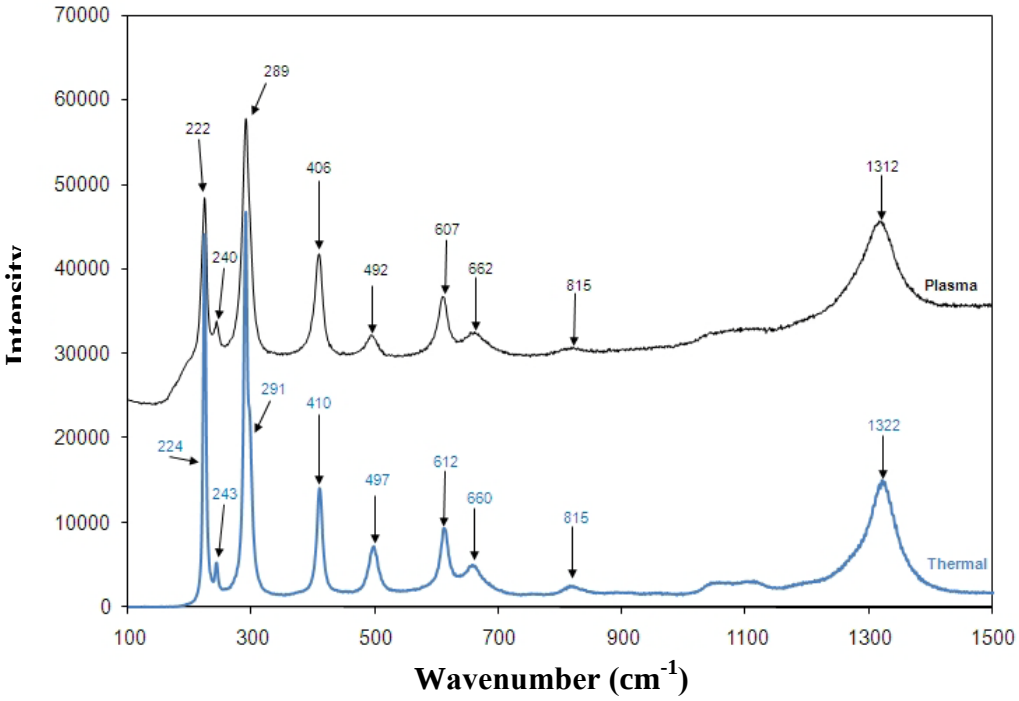

Figure 14. Raman on NWs grown by O_2 plasma oxidation.

Photoluminescence

Low temperature visible-range photoluminescence performed on O_2 plasma synthesized NWs (Figure 15) shows two distinct energy levels at 2.05 and 2.15 eV.

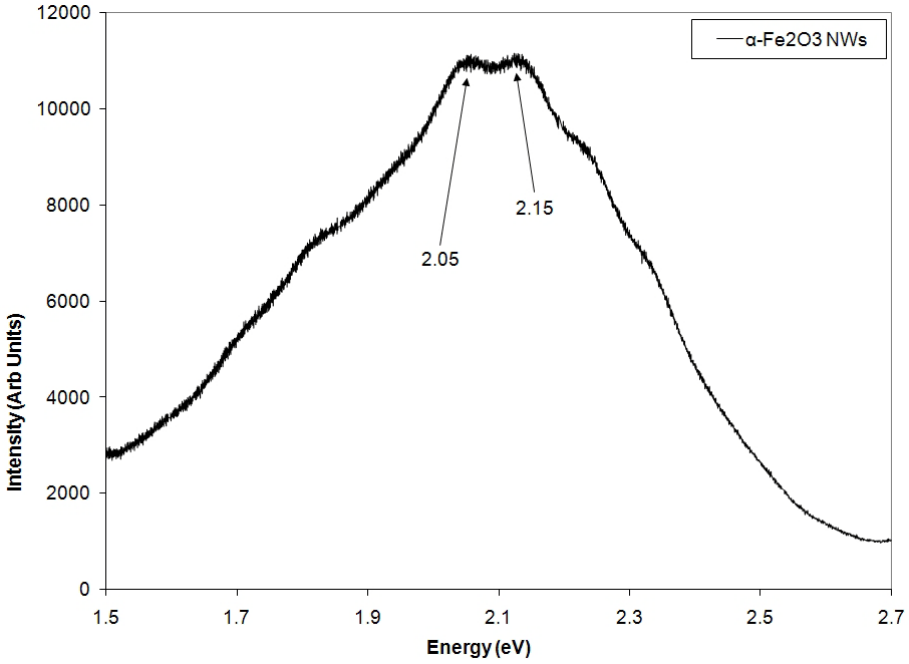

Figure 15. Cold photoluminescence on α-Fe_2O_3 synthesized by O2 plasma oxidation.

UV-Vis

UV-Vis spectroscopy was performed to characterize the band gap of the α-Fe_2O_3 NWs. It was necessary to use diffuse reflectance scans because the samples were opaque. The diffuse reflectance data was converted to absorbance using Equation (12):

$$A = R_{max} - R \tag{12}$$

where R_{max} is the maximum R value beyond the dip in diffuse reflectance. With this formula, the maximum absorbance is set to zero where the curve representing the band

gap dips. The band gap is then determined by extrapolating the straight portion of the curve. This method is discussed further in reference [138]. Figure 16a shows the converted absorbance plot with the long wavelength edge extrapolated to E_g = 2.1 eV, which is in agreements with previously reported estimates[59, 139]. Another method for determining the band gap is based on the absorption coefficient, α:

$$\alpha E_{hv} = A(E_{hv} - E_g)^m \quad (13)$$

$$\therefore (\alpha E_{hv})^{\frac{1}{m}} \propto (E_{hv} - E_g) \quad (14)$$

where A is a constant, Ehv is the energy (eV) of an impinging photon, Eg is the band gap, and m is a constant depending on the type of transition (½ for direct and 2 for indirect). The absorption coefficient is determined by normalizing A to material thickness. It is unclear, in this case, whether the material thickness would correspond to the dimensions of the NWs, or if it would include the underlying oxide or metallic layers. The normalization would contribute a constant to relation (14), keeping the proportionality true. Tauc plots for both direct and indirect transitions for the same wavelength were calculated and are shown in Figure 16b (inset = indirect). Normally, the plot that is more accurately extrapolated with a straight line represents the band gap, but the difference in this case is minimal. The band gap nature of Fe_2O_3 has been debated in many publications and it is generally agreed that it has an indirect transition at around 2.1 eV due to the spin-forbidden Fe^{3+} 3d→3d excitation[48]. It is thus safe to say that these samples also exhibit an indirect band gap of 2.1 eV.

Similarly, an absorbance plot was calculated from the diffuse reflectance data for thermal oxidation. Two significant dips in absorption were observed correlating to 2.09

eV and 1.63 eV. The first is the expected indirect band gap for hematite, but the lower energy transition is unexpected. One possible explanation is the presence of mixed phases due to partial oxidation.

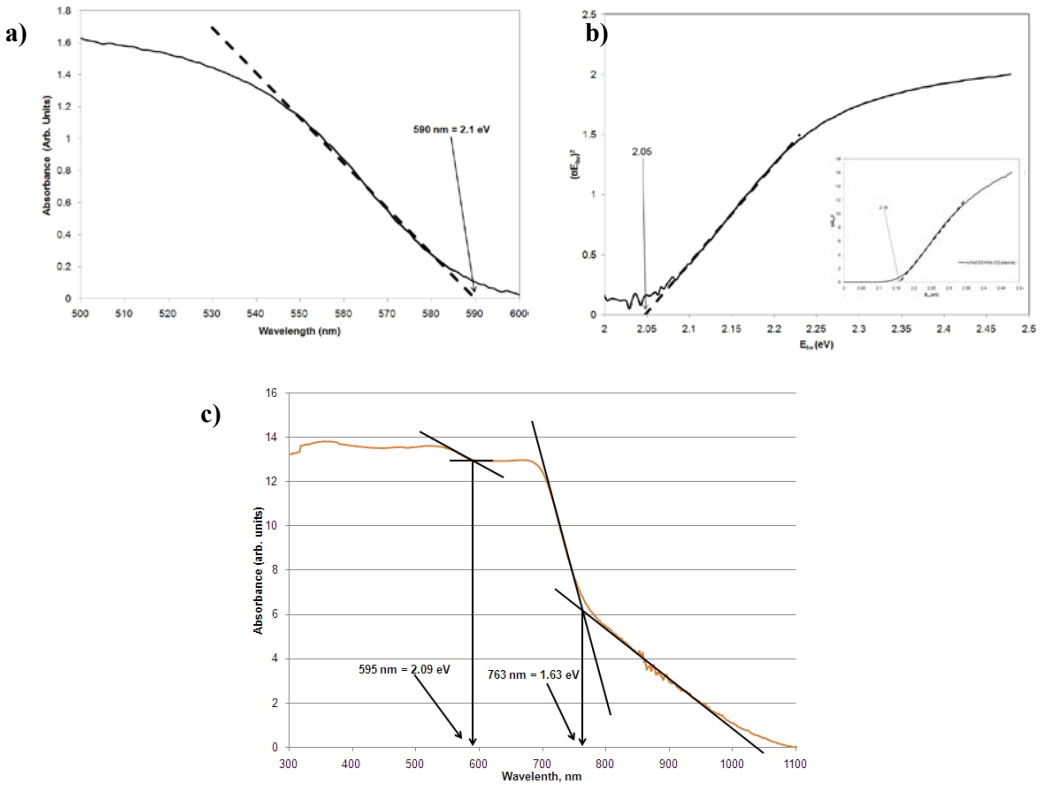

Figure 16. UV-Vis plots estimating band gap of Fe2O3 samples: absorbance plots for (a) plasma oxidized and (c) thermally oxidized samples, and Tauc plots (b) for plasma oxidized samples (large graph is for direct and inset is for indirect transition).

Conductivity Type: Open Circuit Potential

Open circuit potential (OCP) measurements were conducted in order to determine the conductivity type of the electrodes (n- or p-type). When going from darkness to illumination, if the potential of the working electrode decreases (more negative), then it is an n-type semiconductor.

The first half of the OCP curves occurred under dark conditions and the transition represents when the light was turned on. These are presented in Figure 17. The solution was 1M KOH in all the tests. The samples synthesized by O_2 plasma (a) showed an n-type behavior, repeatedly. The absolute value of the potentials shifted positively with each successive OCP trial. This could be due to slow equilibration of the Helmholtz layer and/or slow kinetics for charge transfer across the surface. Samples synthesized by thermal oxidation (b) in air, however, seemed to exhibit p-type behavior. This was a peculiar finding because no doping had been done. Suspecting a surface impurity effect, the samples which were used for UPS—which thus spent much time under ultra high vacuum—were tested for OCP. Consecutive OCP measurements revealed that a transition from n-type behavior to p-type behavior occurred during the scans, as can be seen in (c). After p-type behavior was observed, the sample was then placed in a vacuum chamber (~0.1 torr) overnight. The very next OCP scan (d) again showed n-type behavior, which diminished with further consecutive runs.

N-to-p-type (and p-to-n) transitions have been reported for metallic oxides in the past, attributed to a variety of surface chemistry reactions[140-145]. It is known that metal oxides are capable of chemisorptions of gaseous species at the surface due to oxygen vacancies and surface states[146]. This is likewise true for liquid medium. In solution, the material surface is functionlized with OH groups[147]. The n-to-p-type transition of α-Fe2O3 has been explained by the adsorption of oxygen groups on the surface, which increases band bending to the point that the Fermi level is nearer the valence band than the conduction band at the surface—a condition that exists for p-type semiconductors. Although this explanation is offered, it cannot be readily accepted. It

has been argued that surface chemisorption on semiconductors in liquid medium changes the energies of the surface and has the effect of unpinning the band edges. Furthermore, the potential shift observed in OCP is due to the flattening of bands upon illumination. The direction of the flattening is opposite to that of the bending which occurs when the Fermi levels equilibriate. In other words, even if the bands bend so much that the Fermi level approaches nearer to the minority band edge, the shift observed in OCP upon illumination should still be in the opposite direction of bending. This phenomenon needs to be studied further.

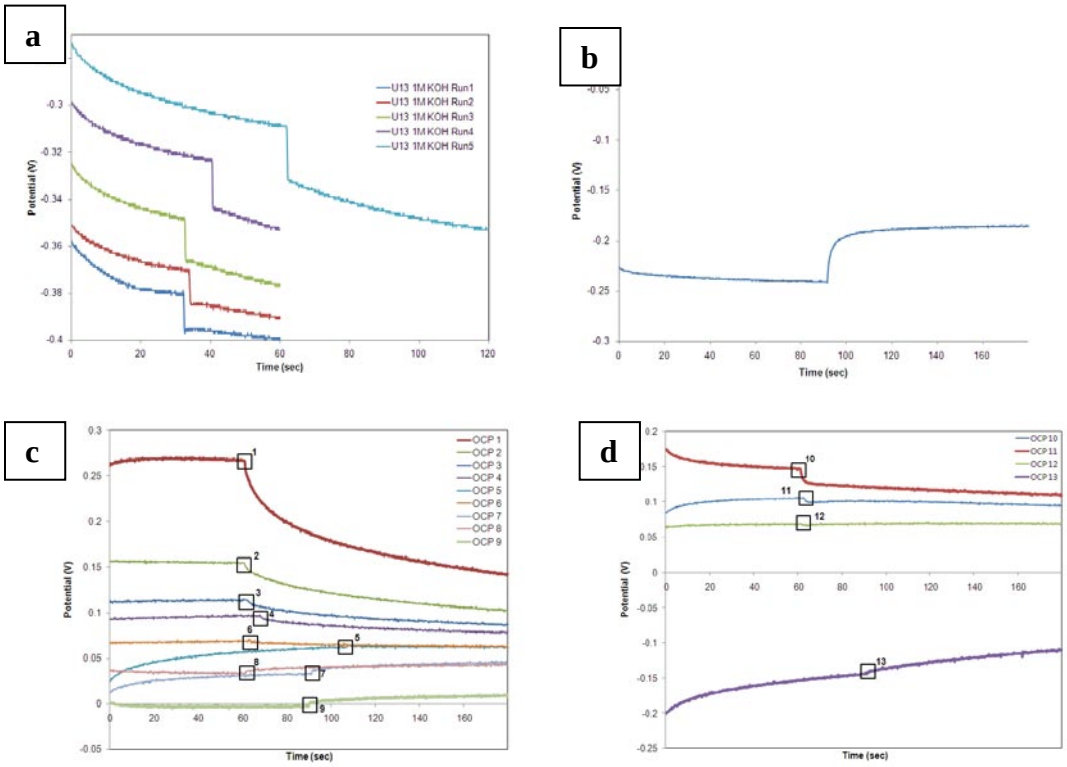

Figure 17. (a) O_2, progressive OCP. Consecutive shifts positive. (b) thermal, OCP, p-type. (c) consecutive, thermal, n to p. (d) consecutive (after vacuum after c), n to p.

UPS

Another test that may determine conductivity type is UPS. In the high kinetic energy (KE), the onset of data corresponds to the Fermi level position in a material. An offset between the gold onset and that of the material of interest correlates to the energy gap between the valence band maximum and the Fermi level. A Helium 1 scan for gold and a thermally oxidized sample are shown in Figure 18. UPS measurement scans on gold and hematite using He 1 excitation.. The 1.6 eV offset confirms that the thermally oxidized iron oxide samples are n-type.

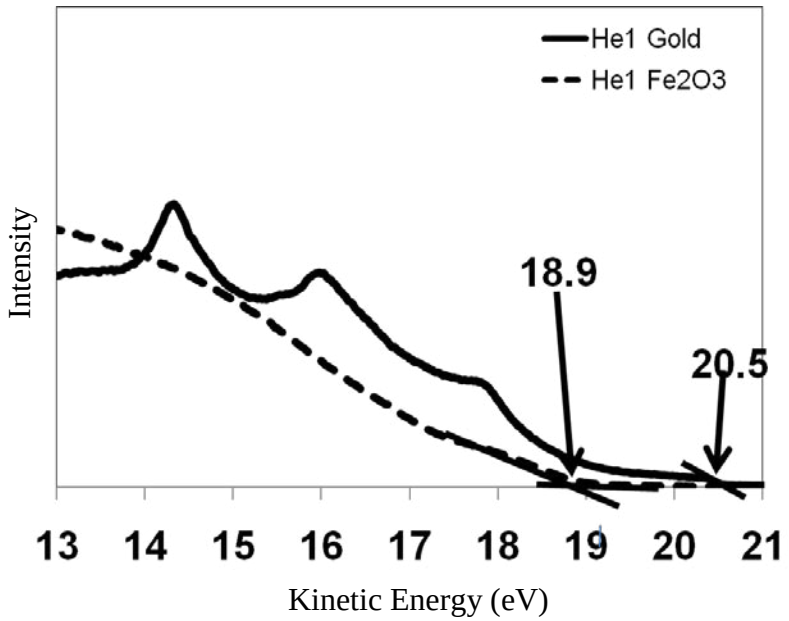

Figure 18. UPS measurement scans on gold and hematite using He 1 excitation.

J-V

As discussed before, reverse bias (positive for n-type) is applied to semiconductors to induce water splitting if the bands do not straddle the redox potentials of hydrogen and oxygen evolution. A forward bias shifts the Fermi level into the majority carrier band (conduction for n-type), which leads to an accumulation of majority carriers at the surface. At this point, the material exhibits metallic conductivity and no photoactivity. As another test of whether the thermally oxidized samples may have p-type conductivity, J-V scans were conducted in the forward bias direction (negative), with the results shown in Figure 19. The dark and light curves are nearly identical and crisscross each other several times, indicating a lack of photoactivity. Furthermore, the two humps between at -0.55 and -0.82 V may be due to the corrosion of iron oxide by reduction. This is supported by the fact that when the samples were removed from solution, new oxidation was seen throughout the electrode surface, and subsequent J-V

tests in the reverse direction produced no photoactivity at all. This did not occur for the samples which were instead reverse biased (discussed below). Therefore, it was concluded that the thermally oxidized electrodes are n-type. The phenomenon observed in OCP measurements deserves further study, however.

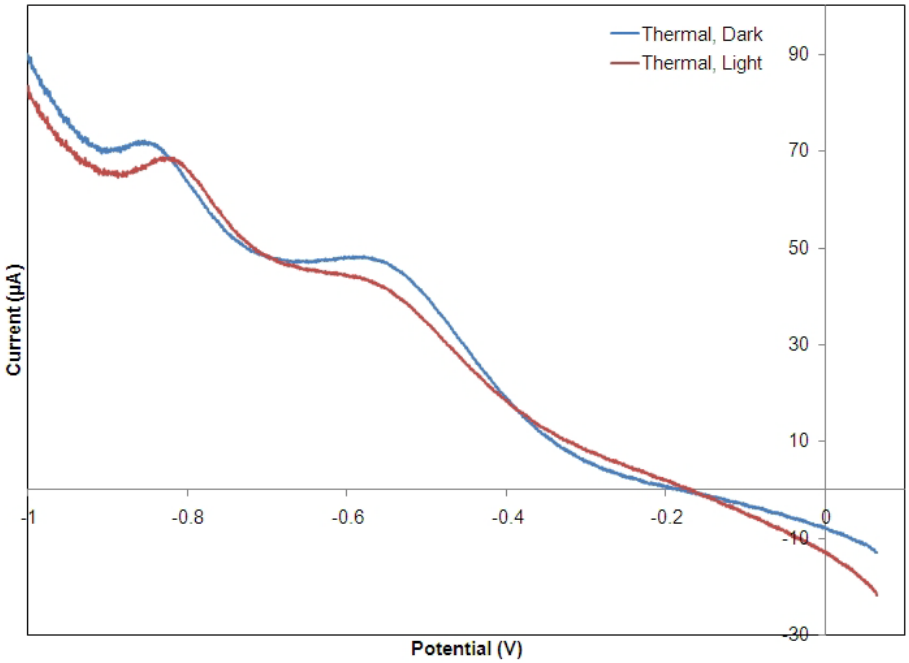

Figure 19. J-V dark and light curves for forward bias of thermally oxidized hematite. Shape of curves indicates photocorrosion and no photoactivity.

J-V measurements comparing the photoactivity of plasma and thermally oxidized electrodes are shown in Figure 20. The curves for the plasma oxidized samples were performed versus SCE (+0.241 V vs. NHE), and the other curves were performed using Ag/AgCl reference electrode (+0.207 V vs. NHE). In Figure 20, all the data was adjusted to match the scale of the plasma oxidized samples (vs. SCE). Dark and light scans are shown for each type. Consistently, the photocurrent onset in all cases is-0.3 V vs. SCE, which indicates that the flat band potential is the same for all three types of samples. The plasma oxidized sample produced much greater photocurrent, however, than the

thermally oxidized samples or the NPs. At +0.3 V vs. SCE, the photocurrent was 255, 2.6, 11.2 $\mu A/cm^2$ for the plasma, thermal, and NP samples, respectively. In all cases, the dark current onset was between +0.4 and 0.5 V vs. SCE. For the NW samples (plasma and thermal), the light current was considerably greater than the dark current even past this point, indicating considerable photoactivity. The dark onset normally corresponds to inversion due to external bias, however, and therefore is not an interesting region for operation in practical applications. The light and dark curves were nearly identical past the dark onset for the NP samples.

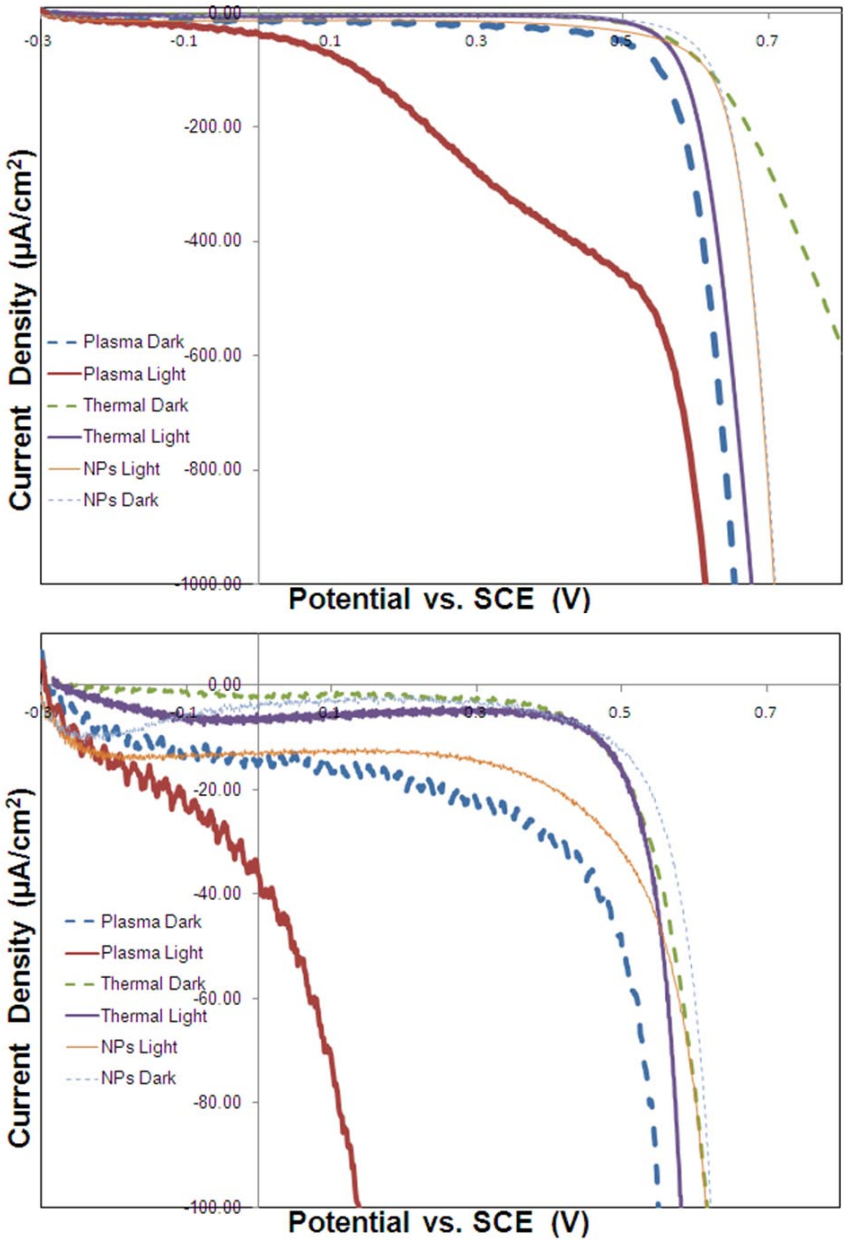

Figure 20. J-V dark and light curves for three types of samples: plasma oxidized, thermally oxidized, and NPs on FTO. The two parts are identical except in the current range plotted. Plasma oxidized samples showed the greatest photocurrent.

These results suggest that the plasma oxidation method is better for producing hematite electrodes capable of photoelectrochemical water splitting than thermal oxidation. In order to understand the drastic difference between the two types of

samples, the interface between the nanowire layer and the iron substrate was analyzed. This was done by scratching the samples and then checking the exposed layers with EDS for presence oxide. This is shown in Figure 21, where part (a) is for the plasma samples and part (b) is for the thermal samples. Scratching reveals the presence of several layers: a top layer upon which the nanostructure grow, a middle layer, and a bottom layer. For the plasma samples, EDS scans show that the presence of oxidized iron in the top layer and at the top of the middle layer, but not below. This suggests that only the full top layer is oxidized iron, while the middle and below layers are pure iron. For the thermal samples, however, the middle layer also shows a strong presence of oxygen, suggesting that the whole region is oxide. From the SEM images—(c) for plasma and (d) for thermal—the thickness of the total oxide layer layers is determined to be about 1 μm and 7.5 μm for the plasma and thermal samples, respectively.

The interfacial layer is detrimental to PEC performance. Other studies have also reported the presence of an interfacial layer between the iron substrate and the hematite surface when grown by direct oxidation[111, 148]. It was shown to be an amorphous layer comprised of Fe3O4 (magnetite) and FeO (wüstite)[149-151]. Due to the mixed phase and poor quality of this layer, charge carriers generated in the surface hematite nanostructures are lost to recombination. Therefore, the advantages offered by the nanowire morphology are negated in the interfacial layer. The large thickness of the interfacial layer in the thermally oxidized samples may thus be an explanation for the poor photoactivity, despite the presence of hematite nanowires on the surface, making it even less photoactive than the NP samples.

The interfacial layer resulting from plasma oxidation may be different than from the well studied thermal oxidation process. Growth of a hematite layer by thermal oxidation is a slow process taking several hours, at the minimum. Hematite can be grown very quickly—in a matter of minutes or seconds—by plasma oxidation, however. Typically that fast processing may lead to metastable phases whereas slow processing leads to equilibrium conditions. A well known example is behavior of iron and carbon during the making of steel. Hot iron is quenched quickly in order to capture more carbon in the iron lattice, to produce tougher steel. In the mechanism proposed for plasma oxidation, initial expose to plasma causes spontaneous iron oxide nucleation at the immediately at the iron-plasma interface. The nanowires were grown when the temperature was near that of the Fe-O phase-transition for hematite, but below 780C, in which case the limited mobility of the iron atoms allows for growth to occur only at the nuclei-metal interface. The original nuclei form the tip of the growing nanowires. There is minimal oxide layer below the body of the continuously growing nanowires and the metal substrate. During shutdown, however, the conditions for growth are lost and during the cooling process an oxide interface may form because of the trapped immobile O-atoms. All this occurs in a matter of seconds. Plasma oxidation does not follow the same growth process as the slower thermal oxidation, in which growth of Fe2O3 is preceded by the development of Fe3O4, which is preceded by an FeO layer. The long duration of thermal oxidation experiments gives more time for the diffusion of O-species farther below the surface of the iron substrate. Further analysis of the interfacial layer is currently underway to establish which oxide phases are present in the interface layer of plasma oxidized samples.

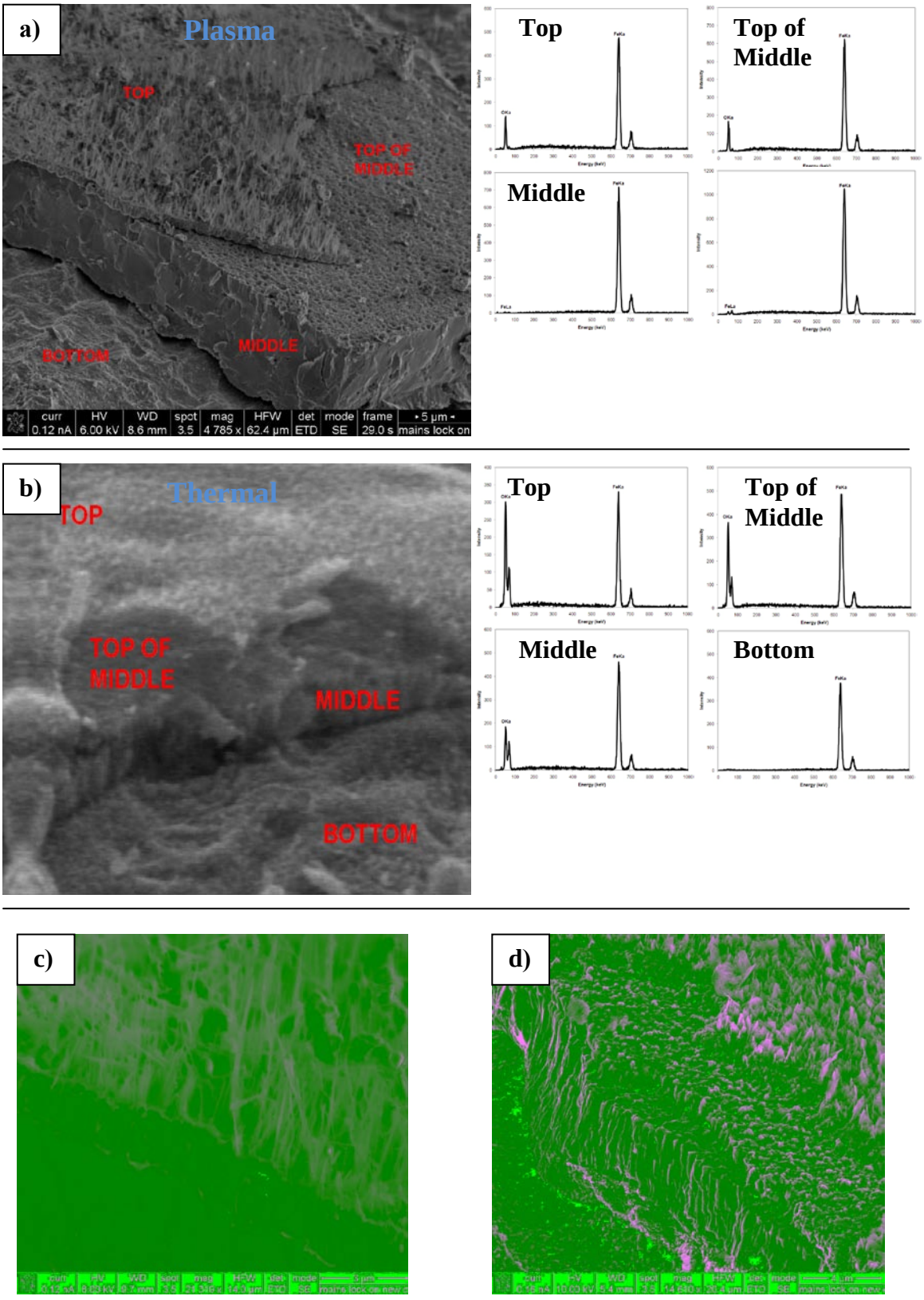

Figure 21. A study of the interfacial iron oxide interfacial layer for plasma (a, c) and thermally (b, d) oxidized samples. The interfacial layer is 1 µm and 7.5 µm for the plasma and thermal samples, respectively.

These data show that plasma oxidation may be the best route for producing hematite samples for solar hydrogen applications. The material may still benefit from the findings of previous studies, such as by the surface treatment with fluorine to raise the shift the conduction band negatively. These studies should be performed on hematite synthesized by plasma oxidation, however.

V. CONCLUSIONS

- Hematite is an excellent material for photoelectrochemical electrolysis because of its 2 eV band gap, wide abundance, and low cost. Nanowire morphologies offer further benefits, including high crystallinity, high surface area, ordered oxygen vacancies parallel to the growth direction, and an excellent substrate for doping studies.
- Hematite (α-Fe_2O_3) nanowire arrays were grown on Fe sheets by direct plasma oxidation and by direct thermal oxidation. The plasma oxidation method takes seconds, whereas thermal oxidation requires several hours.
- UV-Vis measurements confirmed a 2.1 eV band gap for both types of samples. Thermally oxidized samples also showed a transition at 1.63 eV, which may be due to the presence of mixed phases.
- Open circuit potential tests confirmed that the plasma oxidized samples were n-type. OCP measurements show a transition from n-type to p-type behavior over time for thermally oxidized samples. N-type conductivity was confirmed by ultraviolet spectroscopy and by current-voltage measurements, however. The phenomenon observed in the OCP measurements is not yet understood.
- The nanowire arrays grown by plasma oxidation showed far superior photoactivity than those grown by thermal oxidation. This is attributed to the presence of a thick mixed-phase interfacial layer where charge carriers are lost due to recombination. The plasma oxidized samples had a much smaller interfacial layer. The composition of the interfacial layer in plasma oxidized samples is currently being analyzed.

- It is concluded that plasma oxidation should be used to produce hematite samples for studying photoelectrochemical performance.

VI. RECOMMENDATIONS

- The phenomenon responsible for the n-to-p-type behavior in OCP measurements may be interesting and beneficial to analyze and explain.
- The interfacial layer in plasma oxidized hematite should be characterized because the different growth mechanism may mean that this layer is far different than that observed in thermally grown samples.

VII. REFERENCES

[1] N. S. Lewis, "Powering the planet," *Mrs Bulletin,* vol. 32, pp. 808-820, Oct 2007.

[2] Anonymous, "British Petroleum Statistical Review of World Energy," 2009, p. 42.

[3] A. J. Bard, G. M. Whitesides, R. N. Zare, and F. W. McLafferty, "Holy Grails in Chemistry," *Accounts of Chemical Research,* vol. 28, pp. 91-91, Mar 1995.

[4] A. J. Bard and M. A. Fox, "Artificial Photosynthesis - Solar Splitting of Water to Hydrogen and Oxygen," *Accounts of Chemical Research,* vol. 28, pp. 141-145, Mar 1995.

[5] K. Emery and D. Myers, "Reference Solar Spectral Irradiance: Air Mass 1.5." vol. 2009, R. E. R. D. Center, Ed.: National Renewable Energy Laboratory, 2009.

[6] D. Neaman, *An Introduction to Semiconductor Devices*: McGraw-Hill, 2006.

[7] A. J. Nozik and R. Memming, "Physical chemistry of semiconductor-liquid interfaces," *Journal of Physical Chemistry,* vol. 100, pp. 13061-13078, Aug 1996.

[8] A. W. Bott, "Electrochemistry of Semiconductors," *Current Separations,* vol. 17, 1998.

[9] H. Z. Gerischer, *Physcal Chemistry (Munich),* vol. 26, p. 223, 1960.

[10] H. Z. Gerischer, *Physcal Chemistry (Munich),* vol. 27, p. 48, 1961.

[11] A. J. Nozik, "PHOTOELECTROCHEMISTRY - APPLICATIONS TO SOLAR-ENERGY CONVERSION," *Annual Review of Physical Chemistry,* vol. 29, pp. 189-222, 1978.

[12] T. Bak, J. Nowotny, M. Rekas, and C. C. Sorrell, "Photo-electrochemical hydrogen generation from water using solar energy. Materials-related aspects," *International Journal of Hydrogen Energy,* vol. 27, pp. 991-1022, Oct 2002.

[13] H. Gerischer, "Solar photoelectrolysis with semiconductor electrodes," in *Topics in Applied Physics*. vol. 31: Springer, 1979, pp. 115-172.

[14] O. Khaselev and J. A. Turner, "A monolithic photovoltaic-photoelectrochemical device for hydrogen production via water splitting," *Science,* vol. 280, pp. 425-427, Apr 1998.

[15] O. K. Varghese and C. A. Grimes, "Appropriate strategies for determining the photoconversion efficiency of water photo electrolysis cells: A review with examples using titania nanotube array photoanodes," *Solar Energy Materials and Solar Cells,* vol. 92, pp. 374-384, Apr 2008.

[16] A. Fujishima and K. Honda, "Electrochemical Photolysis of Water at a Semiconductor Electrode," *Nature,* vol. 238, pp. 37-+, 1972.

[17] D. H. Kim and M. A. Anderson, "PHOTOELECTROCATALYTIC DEGRADATION OF FORMIC-ACID USING A POROUS TIO2 THIN-FILM ELECTRODE," *Environmental Science & Technology,* vol. 28, pp. 479-483, Mar 1994.

[18] A. L. Linsebigler, G. Q. Lu, and J. T. Yates, "PHOTOCATALYSIS ON TIO2 SURFACES - PRINCIPLES, MECHANISMS, AND SELECTED RESULTS," *Chemical Reviews,* vol. 95, pp. 735-758, May 1995.

[19] J. Nowotny, T. Bak, M. K. Nowotny, and L. R. Sheppard, "Titanium dioxide for solar-hydrogen I. Functional properties," 2007, pp. 2609-2629.

[20] R. van de Krol, A. Goossens, and J. Schoonman, "Mott-Schottky analysis of nanometer-scale thin-film anatase TiO2 (vol 144, pg 1723, 1997)," *Journal of the Electrochemical Society*, vol. 145, pp. 3697-3697, Oct 1998.

[21] H. Rensmo, H. Lindstrom, S. Sodergren, A. K. Willstedt, A. Solbrand, A. Hagfeldt, and S. E. Lindquist, "Photocurrent losses in Nanocrystalline/Nanoporous TiO2 electrodes due to electrochemically active species in the electrolyte," *Journal of the Electrochemical Society*, vol. 143, pp. 3173-3178, Oct 1996.

[22] S. U. M. Khan and T. Sultana, "Photoresponse of n-TiO2 thin film and nanowire electrodes," *Solar Energy Materials and Solar Cells*, vol. 76, pp. 211-221, 2003.

[23] V. M. Aroutiounian, V. M. Arakelyan, and G. E. Shahnazaryan, "Metal oxide photoelectrodes for hydrogen generation using solar radiation-driven water splitting," *Solar Energy*, vol. 78, pp. 581-592, 2005.

[24] J. H. Park, S. Kim, and A. J. Bard, "Novel carbon-doped TiO2 nanotube arrays with high aspect ratios for efficient solar water splitting," *Nano Letters*, vol. 6, pp. 24-28, 2006.

[25] J. Jitputti, Y. Suzuki, and S. Yoshikawa, "Synthesis of TiO2 nanowires and their photocatalytic activity for hydrogen evolution," *Catalysis Communications*, vol. 9, pp. 1265-1271, 2008.

[26] R. van de Krol, Y. Q. Liang, and J. Schoonman, "Solar hydrogen production with nanostructured metal oxides," *Journal of Materials Chemistry*, vol. 18, pp. 2311-2320, May 2008.

[27] K. L. Hardee and A. J. Bard, "SEMICONDUCTOR ELECTRODES .1. CHEMICAL VAPOR-DEPOSITION AND APPLICATION OF POLYCRYSTALLINE N-TYPE TITANIUM-DIOXIDE ELECTRODES TO PHOTOSENSITIZED ELECTROLYSIS OF WATER," *Journal of the Electrochemical Society*, vol. 122, pp. 739-742, 1975.

[28] S. Mathur, V. Sivakov, H. Shen, S. Barth, C. Cavelius, A. Nilsson, and P. Kuhn, "Nanostructured films of iron, tin and titanium oxides by chemical vapor deposition," 2006, pp. 88-93.

[29] A. D. Ogden, J. L. Gole, and A. G. Fedorov, "Optical and electronic properties of semiconducting nanostructures for photocatalytic hydrogen generation," *Journal of Nanoelectronics and Optoelectronics*, vol. 2, pp. 269-277, Dec 2007.

[30] M. Gratzel, "Photoelectrochemical cells," *Nature*, vol. 414, pp. 338-344, Nov 2001.

[31] S. Hotchandani and P. V. Kamat, "PHOTOELECTROCHEMISTRY OF SEMICONDUCTOR ZNO PARTICULATE FILMS," *Journal of the Electrochemical Society*, vol. 139, pp. 1630-1634, Jun 1992.

[32] T. F. Jaramillo, S. H. Baeck, A. Kleiman-Shwarsctein, K. S. Choi, G. D. Stucky, and E. W. McFarland, "Automated electrochemical synthesis and photoelectrochemical characterization of Zn1-xCoxO thin films for solar hydrogen production," *Journal of Combinatorial Chemistry*, vol. 7, pp. 264-271, Mar-Apr 2005.

[33] K. S. Ahn, S. Shet, T. Deutsch, C. S. Jiang, Y. F. Yan, M. Al-Jassim, and J. Turner, "Enhancement of photoelectrochemical response by aligned nanorods in ZnO thin films," *Journal of Power Sources*, vol. 176, pp. 387-392, 2008.

[34] S. H. Baeck, K. S. Choi, T. F. Jaramillo, G. D. Stucky, and E. W. McFarland, "Enhancement of photocatalytic and electrochromic properties of electrochemically fabricated mesoporous WO3 thin films," *Advanced Materials,* vol. 15, pp. 1269-+, Aug 2003.

[35] L. Y. Su, L. G. Zhang, J. H. Fang, M. H. Xu, and Z. H. Lu, "Electrochromic and photoelectrochemical behavior of electrodeposited tungsten trioxide films," *Solar Energy Materials and Solar Cells,* vol. 58, pp. 133-140, Jun 1999.

[36] S. H. Baeck, T. Jaramillo, G. D. Stucky, and E. W. McFarland, "Controlled electrodeposition of nanoparticulate tungsten oxide," *Nano Letters,* vol. 2, pp. 831-834, Aug 2002.

[37] B. Marsen, E. L. Miller, D. Paluselli, and R. E. Rocheleau, "Progress in sputtered tungsten trioxide for photoelectrode applications," 2007, pp. 3110-3115.

[38] M. A. Gondal, A. Hameed, and Z. H. Yamani, "Laser induced photocatalytic splitting of water over WO3 catalyst," *Energy Sources,* vol. 27, pp. 1151-1165, Sep 2005.

[39] J. G. Mavroides, J. A. Kafalas, and D. F. Kolesar, "PHOTOELECTROLYSIS OF WATER IN CELLS WITH SRTIO3 ANODES," *Applied Physics Letters,* vol. 28, pp. 241-243, 1976.

[40] T. Watanabe, A. Fujishima, and K. Honda, "PHOTOELECTROCHEMICAL REACTIONS AT SRTIO3 SINGLE-CRYSTAL ELECTRODE," *Bulletin of the Chemical Society of Japan,* vol. 49, pp. 355-358, 1976.

[41] M. Y. El Zayat, A. O. Saed, and M. S. El-Dessouki, "Photoelectrochemical properties of dye sensitized Zr-doped SrTiO3 electrodes," *International Journal of Hydrogen Energy,* vol. 23, pp. 259-266, Apr 1998.

[42] M. S. Wrighton, A. B. Ellis, P. T. Wolczanski, D. L. Morse, H. B. Abrahamson, and D. S. Ginley, "STRONTIUM-TITANATE PHOTOELECTRODES - EFFICIENT PHOTOASSISTED ELECTROLYSIS OF WATER AT ZERO APPLIED POTENTIAL," *Journal of the American Chemical Society,* vol. 98, pp. 2774-2779, 1976.

[43] A. Derbal, S. Omeiri, A. Bouguelia, and M. Trari, "Characterization of new heterosystem CuFeO2/SnO2 application to visible-light induced hydrogen evolution," *International Journal of Hydrogen Energy,* vol. 33, pp. 4274-4282, Aug 2008.

[44] N. Beermann, L. Vayssieres, S. E. Lindquist, and A. Hagfeldt, "Photoelectrochemical studies of oriented nanorod thin films of hematite," *Journal of the Electrochemical Society,* vol. 147, pp. 2456-2461, Jul 2000.

[45] D. Benjelloun, J. P. Bonnet, J. P. Doumerc, J. C. Launay, M. Onillon, and P. Hagenmuller, "ANISOTROPY OF THE ELECTRICAL-PROPERTIES OF IRON-OXIDE ALPHA-FE2O3," *Materials Chemistry and Physics,* vol. 10, pp. 503-518, 1984.

[46] U. Bjorksten, J. Moser, and M. Gratzel, "PHOTOELECTROCHEMICAL STUDIES ON NANOCRYSTALLINE HEMATITE FILMS," *Chemistry of Materials,* vol. 6, pp. 858-863, Jun 1994.

[47] I. Cesar, A. Kay, J. A. G. Martinez, and M. Gratzel, "Translucent thin film Fe2O3 photoanodes for efficient water splitting by sunlight: Nanostructure-directing

effect of Si-doping," *Journal of the American Chemical Society,* vol. 128, pp. 4582-4583, Apr 2006.

[48] A. Duret and M. Gratzel, "Visible light-induced water oxidation on mesoscopic alpha-Fe2O3 films made by ultrasonic spray pyrolysis," *Journal of Physical Chemistry B,* vol. 109, pp. 17184-17191, Sep 2005.

[49] J. A. Glasscock, P. R. F. Barnes, I. C. Plumb, and N. Savvides, "Enhancement of photoelectrochemical hydrogen production from hematite thin films by the introduction of Ti and Si," *Journal of Physical Chemistry C,* vol. 111, pp. 16477-16488, Nov 2007.

[50] Y. S. Hu, A. Kleiman-Shwarsctein, A. J. Forman, D. Hazen, J. N. Park, and E. W. McFarland, "Pt-doped alpha-Fe2O3 thin films active for photoelectrochemical water splitting," *Chemistry of Materials,* vol. 20, pp. 3803-3805, Jun 2008.

[51] Y. S. Hu, A. Kleiman-Shwarsctein, G. D. Stucky, and E. W. McFarland, "Improved photoelectrochemical performance of Ti-doped alpha-Fe2O3 thin films by surface modification with fluoride," *Chemical Communications,* pp. 2652-2654, 2009.

[52] W. B. Ingler and S. U. M. Khan, "Photoresponse of spray pyrolytically synthesized magnesium-doped iron(III) oxide (p-Fe2O3) thin films under solar simulated light illumination," *Thin Solid Films,* vol. 461, pp. 301-308, Aug 2004.

[53] W. B. Ingler and S. U. M. Khan, "Photoresponse of spray pyrolytically synthesized copper-doped p-Fe2O3 thin film electrodes in water splitting," *International Journal of Hydrogen Energy,* vol. 30, pp. 821-827, Jul 2005.

[54] W. B. Ingler and S. U. M. Khan, "A self-driven p/n-Fe2O3 tandem photoelectrochemical cell for water splitting," *Electrochemical and Solid State Letters,* vol. 9, pp. G144-G146, 2006.

[55] N. Iordanova, M. Dupuis, and K. M. Rosso, "Charge transport in metal oxides: A theoretical study of hematite alpha-Fe2O3," *Journal of Chemical Physics,* vol. 122, p. 10, Apr 2005.

[56] A. Kay, I. Cesar, and M. Gratzel, "New benchmark for water photooxidation by nanostructured alpha-Fe2O3 films," *Journal of the American Chemical Society,* vol. 128, pp. 15714-15721, Dec 2006.

[57] J. H. Kennedy and K. W. Frese, "PHOTOOXIDATION OF WATER AT ALPHA-FE2O3 ELECTRODES," *Journal of the Electrochemical Society,* vol. 124, pp. C130-C130, 1977.

[58] J. H. Kennedy and K. W. Frese, "FLATBAND POTENTIALS AND DONOR DENSITIES OF POLYCRYSTALLINE ALPHA-FE2O3 DETERMINED FROM MOTT-SCHOTTKY PLOTS," *Journal of the Electrochemical Society,* vol. 125, pp. 723-726, 1978.

[59] J. H. Kennedy and K. W. Frese, "PHOTO-OXIDATION OF WATER AT ALPHA-FE2O3 ELECTRODES," *Journal of the Electrochemical Society,* vol. 125, pp. 709-714, 1978.

[60] J. H. Kennedy, M. Anderman, and R. Shinar, "PHOTOACTIVITY OF POLYCRYSTALLINE ALPHA-FE2O3 ELECTRODES DOPED WITH GROUP IVA ELEMENTS," *Journal of the Electrochemical Society,* vol. 128, pp. 2371-2373, 1981.

[61] J. H. Kennedy and M. Anderman, "PHOTOELECTROLYSIS OF WATER AT ALPHA-FE2O3 ELECTRODES IN ACIDIC SOLUTION," *Journal of the Electrochemical Society*, vol. 130, pp. 848-852, 1983.

[62] M. M. Khader, G. H. Vurens, I. K. Kim, M. Salmeron, and G. A. Somorjai, "PHOTOASSISTED CATALYTIC DISSOCIATION OF H2O TO PRODUCE HYDROGEN ON PARTIALLY REDUCED ALPHA-FE2O3," *Journal of the American Chemical Society*, vol. 109, pp. 3581-3585, Jun 1987.

[63] S. U. M. Khan and J. Akikusa, "Photoelectrochemical splitting of water at nanocrystalline n-Fe2O3 thin-film electrodes," *Journal of Physical Chemistry B*, vol. 103, pp. 7184-7189, Aug 1999.

[64] A. Kleiman-Shwarsctein, Y. S. Hu, A. J. Forman, G. D. Stucky, and E. W. McFarland, "Electrodeposition of alpha-Fe2O3 doped with Mo or Cr as photoanodes for photocatalytic water splitting," *Journal of Physical Chemistry C*, vol. 112, pp. 15900-15907, Oct 2008.

[65] S. Kumari, C. Tripathi, A. P. Singh, D. Chauhan, R. Shrivastav, S. Dass, and V. R. Satsangi, "Characterization of Zn-doped hematite thin films for photoelectrochemical splitting of water," *Current Science*, vol. 91, pp. 1062-1064, Oct 2006.

[66] S. Kumari, A. P. Singh, C. Tripathi, D. Chauhan, S. Dass, R. Shrivastav, V. Gupta, K. Sreenivas, and V. R. Satsangi, "Enhanced photoelectrochemical response of Zn-dotted hematite," *International Journal of Photoenergy*, p. 6, 2007.

[67] T. Lindgren, H. L. Wang, N. Beermann, L. Vayssieres, A. Hagfeldt, and S. E. Lindquist, "Aqueous photoelectrochemistry of hematite nanorod array," *Solar Energy Materials and Solar Cells*, vol. 71, pp. 231-243, 2002.

[68] R. K. Quinn, R. D. Nasby, and R. J. Baughman, "PHOTOASSISTED ELECTROLYSIS OF WATER USING SINGLE-CRYSTAL ALPHA-FE2O3 ANODES," *Materials Research Bulletin*, vol. 11, pp. 1011-1017, 1976.

[69] C. J. Sartoretti, M. Ulmann, B. D. Alexander, J. Augustynski, and A. Weidenkaff, "Photoelectrochemical oxidation of water at transparent ferric oxide film electrodes," *Chemical Physics Letters*, vol. 376, pp. 194-200, Jul 2003.

[70] R. Shinar and J. H. Kennedy, "PHOTOACTIVITY OF DOPED ALPHA-FE2O3 ELECTRODES," *Solar Energy Materials*, vol. 6, pp. 323-335, 1982.

[71] K. L. Hardee and A. J. Bard, "SEMICONDUCTOR ELECTRODES .5. APPLICATION OF CHEMICALLY VAPOR-DEPOSITED IRON-OXIDE FILMS TO PHOTOSENSITIZED ELECTROLYSIS," *Journal of the Electrochemical Society*, vol. 123, pp. 1024-1026, 1976.

[72] C. Leygraf, M. Hendewerk, and G. A. Somorjai, "MG-DOPED AND SI-DOPED IRON-OXIDES FOR THE PHOTOCATALYZED PRODUCTION OF HYDROGEN FROM WATER BY VISIBLE-LIGHT (2.2 EV-LESS-THAN-OR-EQUAL-TO-H-NU-LESS-THAN-OR-EQUAL-TO-2.7 EV)," *Journal of Catalysis*, vol. 78, pp. 341-351, 1982.

[73] C. Leygraf, M. Hendewerk, and G. A. Somorjai, "PHOTO-DISSOCIATION OF WATER BY PARA-TYPE AND NORMAL-TYPE POLYCRYSTALLINE IRON-OXIDES BY USING VISIBLE-LIGHT (LESS-THAN-OR-EQUAL-TO 2.7 EV) IN THE ABSENCE OF EXTERNAL POTENTIAL," *Proceedings of the*

National Academy of Sciences of the United States of America-Physical Sciences, vol. 79, pp. 5739-5741, 1982.

[74] M. P. Dareedwards, J. B. Goodenough, A. Hamnett, and P. R. Trevellick, "ELECTROCHEMISTRY AND PHOTOELECTROCHEMISTRY OF IRON(III) OXIDE," *Journal of the Chemical Society-Faraday Transactions I*, vol. 79, pp. 2027-2041, 1983.

[75] K. Itoh and J. O. Bockris, "THIN-FILM PHOTOELECTROCHEMISTRY - IRON-OXIDE," *Journal of the Electrochemical Society*, vol. 131, pp. 1266-1271, 1984.

[76] J. E. Turner, M. Hendewerk, J. Parmeter, D. Neiman, and G. A. Somorjai, "THE CHARACTERIZATION OF DOPED IRON-OXIDE ELECTRODES FOR THE PHOTODISSOCIATION OF WATER - STABILITY, OPTICAL, AND ELECTRONIC-PROPERTIES," *Journal of the Electrochemical Society*, vol. 131, pp. 1777-1783, 1984.

[77] J. K. Leland and A. J. Bard, "PHOTOCHEMISTRY OF COLLOIDAL SEMICONDUCTING IRON-OXIDE POLYMORPHS," *Journal of Physical Chemistry*, vol. 91, pp. 5076-5083, Sep 1987.

[78] A. Bernasik, J. Janowski, W. Hirschwald, F. Stolze, and J. Nowotny, "EFFECT OF SURFACE-TREATMENT ON SEGREGATION OF IMPURITIES IN HEMATITE," *Journal of Materials Science*, vol. 26, pp. 2527-2532, May 1991.

[79] N. Uekawa, M. Watanabe, K. Kaneko, and F. Mizukami, "MIXED-VALENCE FORMATION IN HIGHLY ORIENTED TI-DOPED IRON-OXIDE FILM," *Journal of the Chemical Society-Faraday Transactions*, vol. 91, pp. 2161-2166, Jul 1995.

[80] N. J. Cherepy, D. B. Liston, J. A. Lovejoy, H. M. Deng, and J. Z. Zhang, "Ultrafast studies of photoexcited electron dynamics in gamma- and alpha-Fe2O3 semiconductor nanoparticles," *Journal of Physical Chemistry B*, vol. 102, pp. 770-776, Jan 1998.

[81] K. M. Rosso, D. M. A. Smith, and M. Dupuis, "An ab initio model of electron transport in hematite (alpha-Fe2O3) basal planes," *Journal of Chemical Physics*, vol. 118, pp. 6455-6466, Apr 2003.

[82] A. Watanabe and H. Kozuka, "Photoanodic properties of sol-gel-derived Fe2O3 thin films containing dispersed gold and silver particles," *Journal of Physical Chemistry B*, vol. 107, pp. 12713-12720, Nov 2003.

[83] M. A. Gondal, A. Hameed, Z. H. Yamani, and A. Suwaiyan, "Production of hydrogen and oxygen by water splitting using laser induced photo-catalysis over Fe2O3," *Applied Catalysis a-General*, vol. 268, pp. 159-167, Aug 2004.

[84] V. M. Aroutiounian, V. M. Arakelyan, G. E. Shahnazaryan, G. M. Stepanyan, E. A. Khachaturyan, and J. A. Turner, "Investigations of the structure of the iron oxide semiconductor-electrolyte interface," 2006, pp. 325-331.

[85] T. Arai, Y. Konishi, Y. Iwasaki, H. Sugihara, and K. Sayama, "High-throughput screening using porous photoelectrode for the development of visible-light-responsive semiconductors," *Journal of Combinatorial Chemistry*, vol. 9, pp. 574-581, Jul-Aug 2007.

[86] S. M. Ahmed, J. Leduc, and S. F. Haller, "PHOTOELECTROCHEMICAL AND IMPEDANCE CHARACTERISTICS OF SPECULAR HEMATITE .1.

PHOTOELECTROCHEMICAL, PARALLEL CONDUCTANCE, AND TRAP RATE STUDIES," *Journal of Physical Chemistry,* vol. 92, pp. 6655-6660, Nov 1988.

[87] C. Sanchez, K. D. Sieber, and G. A. Somorjai, "THE PHOTOELECTROCHEMISTRY OF NIOBIUM DOPED ALPHA-FE2(03)," *Journal of Electroanalytical Chemistry,* vol. 252, pp. 269-290, Oct 1988.

[88] C. Leygraf, M. Hendewerk, and G. Somorjai, "THE PREPARATION AND SELECTED PROPERTIES OF MG-DOPED PARA-TYPE IRON-OXIDE AS A PHOTO-CATHODE FOR THE PHOTOELECTROLYSIS OF WATER USING VISIBLE-LIGHT," *Journal of Solid State Chemistry,* vol. 48, pp. 357-367, 1983.

[89] W. B. Ingler, J. P. Baltrus, and S. U. M. Khan, "Photoresponse of p-type zinc-doped iron(III) oxide thin films," *Journal of the American Chemical Society,* vol. 126, pp. 10238-10239, Aug 2004.

[90] Z. Y. Fan, X. G. Wen, S. H. Yang, and J. G. Lu, "Controlled p- and n-type doping of Fe2O3 nanobelt field effect transistors," *Applied Physics Letters,* vol. 87, p. 3, Jul 2005.

[91] V. M. Aroutiounian, V. M. Arakelyan, G. E. Shahnazaryan, G. M. Stepanyan, J. A. Turner, and O. Khaselev, "Investigation of ceramic Fe2O3 < Ta > photoelectrodes for solar energy photoelectrochemical converters," *International Journal of Hydrogen Energy,* vol. 27, pp. 33-38, Jan 2002.

[92] V. M. Aroutiounian, V. M. Arakelyan, G. E. Shahnazaryan, G. M. Stepanyan, E. A. Khachaturyan, H. Wang, and J. A. Turner, "Photoelectrochemistry of semiconductor electrodes made of solid solutions in the system Fe2O3-Nb2O5," *Solar Energy,* vol. 80, pp. 1098-1111, 2006.

[93] C. J. Sartoretti, B. D. Alexander, R. Solarska, W. A. Rutkowska, J. Augustynski, and R. Cerny, "Photoelectrochemical oxidation of water at transparent ferric oxide film electrodes," *Journal of Physical Chemistry B,* vol. 109, pp. 13685-13692, Jul 2005.

[94] D. H. Wu, Z. X. Zhang, L. F. Xu, L. L. Shen, and X. Wang, "Preparation of monodispersed nano alpha-Fe2O3 single crystal particles by refluxing hydrothermal method," *Chinese Journal of Inorganic Chemistry,* vol. 20, pp. 31-36, Jan 2004.

[95] M. Iwasaki, M. Hara, and S. Ito, "Synthesis of nanometer-sized hematite single crystals through NAC-FAS method," *Journal of Materials Science,* vol. 35, pp. 943-949, Feb 2000.

[96] L. S. Zhong, J. S. Hu, H. P. Liang, A. M. Cao, W. G. Song, and L. J. Wan, "Self-assembled 3D flowerlike iron oxide nanostructures and their application in water treatment," *Advanced Materials,* vol. 18, pp. 2426-+, Sep 2006.

[97] H. T. Cui, M. Zayat, and D. Levy, "Sol-gel synthesis of nanoscaled spinels using propylene oxide as a gelation agent," *Journal of Sol-Gel Science and Technology,* vol. 35, pp. 175-181, Sep 2005.

[98] A. E. Gash, T. M. Tillotson, J. H. Satcher, J. F. Poco, L. W. Hrubesh, and R. L. Simpson, "Use of epoxides in the sol-gel synthesis of porous iron(III) oxide monoliths from Fe(III) salts," *Chemistry of Materials,* vol. 13, pp. 999-1007, Mar 2001.

[99] H. Z. Wang, X. T. Zhang, B. Liu, H. L. Zhao, Y. C. Li, Y. B. Huang, and Z. L. Du, "Synthesis and characterization of single crystal alpha-Fe2O3 nanobelts," *Chemistry Letters*, vol. 34, pp. 184-185, Feb 2005.
[100] K. Woo, H. J. Lee, J. P. Ahn, and Y. S. Park, "Sol-gel mediated synthesis of Fe2O3 nanorods," *Advanced Materials*, vol. 15, pp. 1761-+, Oct 2003.
[101] J. Nagahama and H. Yumoto, "Application of Fe oxide films prepared by PVD methods to protect Fe metal from corrosion," 2003, pp. 658-661.
[102] Y. L. Chueh, M. W. Lai, J. Q. Liang, L. J. Chou, and Z. L. Wang, "Systematic study of the growth of aligned arrays of alpha-Fe2O3 and Fe3O4 nanowires by a vapor-solid process," *Advanced Functional Materials*, vol. 16, pp. 2243-2251, Nov 2006.
[103] Z. Q. Chen, U. Cvelbar, M. Mozetic, J. Q. He, and M. K. Sunkara, "Long-range ordering of oxygen-vacancy planes in alpha-Fe2O3 nanowires and nanobelts," *Chemistry of Materials*, vol. 20, pp. 3224-3228, May 13 2008.
[104] U. Cvelbar, Z. Q. Chen, M. K. Sunkara, and M. Mozetic, "Spontaneous Growth of Superstructure alpha-Fe2O3 Nanowire and Nanobelt Arrays in Reactive Oxygen Plasma," *Small*, vol. 4, pp. 1610-1614, Oct 2008.
[105] U. Cvelbar, K. Ostrikov, I. Levchenko, M. Mozetic, and M. K. Sunkara, "Control of morphology and nucleation density of iron oxide nanostructures by electric conditions on iron surfaces exposed to reactive oxygen plasmas," *Applied Physics Letters*, vol. 94, May 25 2009.
[106] L. Vayssieres, J. H. Guo, and J. Nordgren, "Aqueous chemical growth of alpha-Fe2O3-alpha-Cr2O3 nanocomposite thin films," *Journal of Nanoscience and Nanotechnology*, vol. 1, pp. 385-388, Dec 2001.
[107] R. Schrebler, K. Bello, F. Vera, P. Cury, E. Munoz, R. del Rio, H. G. Meier, R. Cordova, and E. A. Dalchiele, "An electrochemical deposition route for obtaining alpha-Fe2O3 thin films," *Electrochemical and Solid State Letters*, vol. 9, pp. C110-C113, 2006.
[108] G. Zotti, G. Schiavon, S. Zecchin, and U. Casellato, "Electrodeposition of amorphous Fe2O3 films by reduction of iron perchlorate in acetonitrile," *Journal of the Electrochemical Society*, vol. 145, pp. 385-389, Feb 1998.
[109] R. Schrebler, C. Llewelyn, F. Vera, P. Cury, E. Munoz, R. del Rio, H. G. Meier, R. Cordova, and E. A. Dalchiele, "An electrochemical deposition route for obtaining alpha-Fe2O3 thin films - II. EQCM study and semiconductor properties," *Electrochemical and Solid State Letters*, vol. 10, pp. D95-D99, 2007.
[110] R. M. Wang, Y. F. Chen, Y. Y. Fu, H. Zhang, and C. Kisielowski, "Bicrystalline hematite nanowires," *Journal of Physical Chemistry B*, vol. 109, pp. 12245-12249, Jun 2005.
[111] Y. Y. Fu, R. M. Wang, J. Xu, J. Chen, Y. Yan, A. Narlikar, and H. Zhang, "Synthesis of large arrays of aligned alpha-Fe2O3 nanowires," *Chemical Physics Letters*, vol. 379, pp. 373-379, Sep 2003.
[112] Q. Han, Y. Y. Xu, Y. Y. Fu, H. Zhang, R. M. Wang, T. M. Wang, and Z. Y. Chen, "Defects and growing mechanisms of alpha-Fe2O3 nanowires," *Chemical Physics Letters*, vol. 431, pp. 100-103, Nov 2006.

[113] J. D. Beach, R. T. Collins, and J. A. Turner, "Band-edge Potentials of n-type and p-type GaN," *Journal of the Electrochemical Society,* vol. 150, pp. A899-A904, Jul 2003.
[114] S. S. Kocha, M. W. Peterson, D. J. Arent, J. M. Redwing, M. A. Tischler, and J. A. Turner, "Electrochemical investigation of the gallium nitride-aqueous electrolyte interface," *Journal of the Electrochemical Society,* vol. 142, pp. L238-L240, Dec 1995.
[115] J. Akikusa and S. U. M. Khan, "Photoelectrolysis of water to hydrogen in p-SiC/Pt and p-SiC/n-TiO2 cells," *International Journal of Hydrogen Energy,* vol. 27, pp. 863-870, Sep 2002.
[116] B. Damilano, N. Grandjean, S. Vezian, and J. Massies, "InGaN heterostructures grown by molecular beam epitaxy: from growth mechanism to optical properties," 2001, pp. 466-470.
[117] I. H. Ho and G. B. Stringfellow, "Solid phase immiscibility in GaInN," *Applied Physics Letters,* vol. 69, pp. 2701-2703, Oct 1996.
[118] J. W. Orton and C. T. Foxon, "Group III nitride semiconductors for short wavelength light-emitting devices," *Reports on Progress in Physics,* vol. 61, pp. 1-+, Jan 1998.
[119] T. Shioda, M. Sugiyama, Y. Shimogaki, and Y. Nakano, "Selective area metal-organic vapor-phase epitaxy of InN, GaN and InGaN covering whole composition range," 2009, pp. 2809-2812.
[120] O. Khaselev and J. A. Turner, "Electrochemical stability of p-GaInP2 in aqueous electrolytes toward photoelectrochemical water splitting," *Journal of the Electrochemical Society,* vol. 145, pp. 3335-3339, Oct 1998.
[121] O. Khaselev and J. A. Turner, "Anodic oxidation of GaInP2," *Corrosion Science,* vol. 42, pp. 1831-1838, Oct 2000.
[122] O. Khaselev, A. Bansal, and J. A. Turner, "High-efficiency integrated multijunction photovoltaic/electrolysis systems for hydrogen production," 2001, pp. 127-132.
[123] T. G. Deutsch, C. A. Koval, and J. A. Turner, "III-V nitride epilayers for photoelectrochemical water splitting: GaPN and GaAsPN," *Journal of Physical Chemistry B,* vol. 110, pp. 25297-25307, Dec 2006.
[124] T. G. Deutsch, J. L. Head, and J. A. Turner, "Photoelectrochemical characterization and durability analysis of GaInPN epilayers," *Journal of the Electrochemical Society,* vol. 155, pp. B903-B907, 2008.
[125] R. E. Rocheleau and E. L. Miller, "Photoelectrochemical production of hydrogen: Engineering loss analysis," *International Journal of Hydrogen Energy,* vol. 22, pp. 771-782, Aug 1997.
[126] J. R. Bolton, "Solar photoproduction of hydrogen: A review," *Solar Energy,* vol. 57, pp. 37-50, Jul 1996.
[127] L. Vayssieres, C. Sathe, S. M. Butorin, D. K. Shuh, J. Nordgren, and J. H. Guo, "One-dimensional quantum-confinement effect in alpha-Fe2O3 ultrafine nanorod arrays," *Advanced Materials,* vol. 17, pp. 2320-+, Oct 2005.
[128] M. Mozetic, U. Cvelbar, M. K. Sunkara, and S. Vaddiraju, "A method for the rapid synthesis of large quantities of metal oxide nanowires at low temperatures," *Advanced Materials,* vol. 17, pp. 2138-+, Sep 2005.

[129] L. Vayssieres, N. Beermann, S. E. Lindquist, and A. Hagfeldt, "Controlled aqueous chemical growth of oriented three-dimensional crystalline nanorod arrays: Application to iron(III) oxides," *Chemistry of Materials,* vol. 13, pp. 233-235, Feb 2001.

[130] T. Yu, Y. W. Zhu, X. J. Xu, K. S. Yeong, Z. X. Shen, P. Chen, C. T. Lim, J. T. L. Thong, and C. H. Sow, "Substrate-friendly synthesis of metal oxide nanostructures using a hotplate," *Small,* vol. 2, pp. 80-84, Jan 2006.

[131] C. H. Kim, H. J. Chun, D. S. Kim, S. Y. Kim, J. Park, J. Y. Moon, G. Lee, J. Yoon, Y. Jo, M. H. Jung, S. I. Jung, and C. J. Lee, "Magnetic anisotropy of vertically aligned alpha-Fe2O3 nanowire array," *Applied Physics Letters,* vol. 89, p. 3, Nov 2006.

[132] X. G. Wen, S. H. Wang, Y. Ding, Z. L. Wang, and S. H. Yang, "Controlled growth of large-area, uniform, vertically aligned arrays of alpha-Fe2O3 nanobelts and nanowires," *Journal of Physical Chemistry B,* vol. 109, pp. 215-220, Jan 2005.

[133] V. Kumar, J. H. Kim, C. Pendyala, B. Chernomordik, and M. K. Sunkara, "Gas-Phase, Bulk Production of Metal Oxide Nanowires and Nanoparticles Using a Microwave Plasma Jet Reactor," *Journal of Physical Chemistry C,* vol. 112, pp. 17750-17754, Nov 2008.

[134] U. Cvelbar, K. Ostrikov, I. Levchenko, M. Mozetic, and M. K. Sunkara, "Control of morphology and nucleation density of iron oxide nanostructures by electric conditions on iron surfaces exposed to reactive oxygen plasmas," *Applied Physics Letters,* vol. 94, May 2009.

[135] H. Matsushima, T. Nohira, I. Mogi, and Y. Ito, "Effects of magnetic fields on iron electrodeposition," *Surface & Coatings Technology,* vol. 179, pp. 245-251, Feb 2004.

[136] F. Ronkel, J. W. Schultze, and R. ArensFischer, "Electrical contact to porous silicon by electrodeposition of iron," 1996, pp. 40-43.

[137] I. Chourpa, L. Douziech-Eyrolles, L. Ngaboni-Okassa, J. F. Fouquenet, S. Cohen-Jonathan, M. Souce, H. Marchais, and P. Dubois, "Molecular composition of iron oxide nanoparticles, precursors for magnetic drug targeting, as characterized by confocal Raman microspectroscopy," *Analyst,* vol. 130, pp. 1395-1403, 2005.

[138] A. B. Murphy, "Band-gap determination from diffuse reflectance measurements of semiconductor films, and application to photoelectrochemical water-splitting," *Solar Energy Materials and Solar Cells,* vol. 91, pp. 1326-1337, Sep 2007.

[139] W. H. Strehlow and E. L. Cook, "Compilation of Energy
Band gaps in Elemental and binary Compound Semiconductors and Insulators," *Journal of Physical and Chemical Reference Data,* vol. 2, pp. 163-185, 1973.

[140] H. Teterycz, B. W. Licznerski, K. Nitsch, K. Wisniewski, and L. J. Golonka, "Anomalous behaviour of new thick film gas sensitive composition," 1998, pp. 153-157.

[141] N. Barsan, R. Grigorovici, R. Ionescu, M. Motronea, and A. Vancu, "MECHANISM OF GAS-DETECTION IN POLYCRYSTALLINE THICK-FILM SNO2 SENSORS," *Thin Solid Films,* vol. 171, pp. 53-63, Apr 1989.

[142] K. Galatsis, L. Cukrov, W. Wlodarski, P. McCormick, K. Kalantar-zadeh, E. Comini, and G. Sberveglieri, "p- and n-type Fe-doped SnO2 gas sensors fabricated by the mechanochemical processing technique," 2003, pp. 562-565.
[143] A. K. Prasad, D. J. Kubinski, and P. I. Gouma, "Comparison of sol-gel and ion beam deposited MoO3 thin film gas sensors for selective ammonia detection," 2003, pp. 25-30.
[144] G. Korotcenkov, V. Brinzari, V. Golovanov, A. Cerneavschi, V. Matolin, and A. Tadd, "Acceptor-like behavior of reducing gases on the surface of n-type In2O3," *Applied Surface Science,* vol. 227, pp. 122-131, Apr 2004.
[145] P. Menini, F. Parret, M. Guerrero, K. Soulantica, L. Erades, A. Maisonnat, and B. Chaudret, "CO response of a nanostructured SnO2 gas sensor doped with palladium and platinum," 2004, pp. 111-114.
[146] N. Barsan and U. Weimar, "Understanding the fundamental principles of metal oxide based gas sensors; the example of CO sensing with SnO2 sensors in the presence of humidity," *Journal of Physics-Condensed Matter,* vol. 15, pp. R813-R839, May 2003.
[147] G. D. Parfitt, "SURFACE-CHEMISTRY OF OXIDES," *Pure and Applied Chemistry,* vol. 48, pp. 415-418, 1976.
[148] P. M. Rao and X. Zheng, "Rapid Catalyst-Free Flame Synthesis of Dense, Aligned α-Fe2O3 Nanoflake and CuO Nanoneedle Arrays," *Nano Letters,* vol. 0.
[149] D. A. Voss, E. P. Butler, and T. E. Mitchell, "THE GROWTH OF HEMATITE BLADES DURING THE HIGH-TEMPERATURE OXIDATION OF IRON," *Metallurgical Transactions a-Physical Metallurgy and Materials Science,* vol. 13, pp. 929-935, 1982.
[150] S. R. J. Saunders, M. Monteiro, and F. Rizzo, "The oxidation behaviour of metals and alloys at high temperatures in atmospheres containing water vapour: A review," *Progress in Materials Science,* vol. 53, pp. 775-837, Jul 2008.
[151] R. Y. Chen and W. Y. D. Yuen, "Review of the high-temperature oxidation of iron and carbon steels in air or oxygen," *Oxidation of Metals,* vol. 59, pp. 433-468, Jun 2003.

VIII. VITA

Boris Chernomordik received his B.S. in Chemical Engineering Summa Cum Laude from the University of Louisville in May 2008. He will pursue a doctoral degree in Chemical Engineering from the University of Minnesota, Twin Cities, with a National Science Foundation Graduate Fellowship.